Microporous and Mesoporous Materials 357 (2023) 112631

Contents lists available at ScienceDirect

Microporous and Mesoporous Materials

journal homepage: www.elsevier.com/locate/micromeso

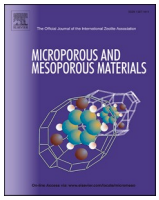

Efficient Xe/Kr separation in fluorinated pillar-caged metal-organic frameworks

Jiahao Li [a], Lingyao Wang [a,**], Yuxin Chen [a], Zonglin Gu [b,***], Tao Jiang [c], Binquan Luan [d,****], Rajamani Krishna [e], Yuanbin Zhang [a,*]

[a] Key Laboratory of the Ministry of Education for Advanced Catalysis Materials, College of Chemistry and Material Sciences, Zhejiang Normal University, Jinhua, 321004, China
[b] College of Physical Science and Technology, Yangzhou University, Jiangsu, 225009, China
[c] Department of Pharmacy, Jiangxi University of Chinese Medicine, Nanchang, 330004, China
[d] IBM Thomas J. Watson Research, Yorktown Heights, NY, 10598, United States
[e] Van't Hoff Institute for Molecular Sciences, University of Amsterdam, Science Park 904, 1098 XH, Amsterdam, Netherlands

ARTICLE INFO

Keywords:
Xe/Kr separation
Fluorinated metal organic frameworks
Gas separation
Anion pillared MOF
Selectivity

ABSTRACT

The separation of xenon/krypton (Xe/Kr) mixture is of great significance in industry, yet challenging due to their close physical properties. Traditional porous materials typically fail to realize a balance between adsorption capacity and selectivity. Herein, we report a series of water stable fluorinated anion pillared metal-organic frameworks (TIFSIX-Cu-TPA, GeFSIX-Cu-TPA and NbOFFIVE-Cu-TPA) with suitable cages for efficient capture/separation of Xe from Kr. The adsorption capacities of TIFSIX-Cu-TPA, GeFSIX-Cu-TPA and NbOFFIVE-Cu-TPA for Xe at 298 K and 1.0 bar are 64.5, 61.2 and 59.0 STP $cm^3\ g^{-1}$, respectively, while those for Kr are only 16.9, 15.8 and 14.9 STP $cm^3\ g^{-1}$. Correspondingly, the IAST selectivities for these MOFs are respectively 5.4, 5.3 and 5.1 at 298 K and 1 bar for the Xe/Kr (20/80) mixtures, superior to those of most popular porous materials in the context of Xe/Kr separation. The adsorption heats for Xe are as modest as 22.3, 21.7 and 21.5 kJ/mol for TIFSIX-Cu-TPA, GeFSIX-Cu-TPA and NbOFFIVE-Cu-TPA respectively, indicating the facile conditions for regeneration of the materials. The Xe/Kr binding sites were further studied by Grand Canonical Monte Carlo (GCMC) simulations and density functional theory (DFT) calculations, indicating the preferred binding with Xe over Kr in the large cages decorated with fluorine atoms, corroborating the experimental results. The practical performance of dynamic Xe/Kr separation is further demonstrated by transient breakthrough simulations and experiments.

1. Introduction

The noble gases xenon (Xe) and krypton (Kr) play an important role in various industrial fields and are dubbed as the "gold gases". Xe and Kr were discovered in the 19th century, and were later widely used in medical imaging, commercial lighting, anesthesia, electronic chips and spacecraft propellants [1–4]. The concentrations of Xe and Kr in the air are only 0.09 and 1.14 ppm, respectively. Xe/Kr (20/80, v/v) mixture can be generally obtained as a byproduct in the separation of nitrogen and oxygen from air [5]. At present, pure Xe and Kr are usually produced by low temperature distillation, which is highly energy-intensive [6]. Therefore, it is urgently and highly demanded to develop alternative technologies to replace the energy-intensive cryogenic distillation process.

In this context, physical adsorption separation based on porous solid adsorbents has attracted increasing attention due to its lower capital, reduced energy consumption and environmental friendliness. However, due to the fact that Xe and Kr exhibit similar physical properties such as the close kinetic diameters (4.05 Å for Xe and 3.65 Å for Kr) and neutral charges, the traditional solid porous materials such as porous carbon and

* Corresponding author.
** Corresponding author.
*** Corresponding author.
**** Corresponding author.
E-mail addresses: lywang@zjnu.edu.cn (L. Wang), guzonglin@yzu.edu.cn (Z. Gu), bluan@us.ibm.com (B. Luan), ybzhang@zjnu.edu.cn (Y. Zhang).

https://doi.org/10.1016/j.micromeso.2023.112631
Received 24 March 2023; Received in revised form 28 April 2023; Accepted 2 May 2023
Available online 3 May 2023

zeolite have low adsorption capacity and selectivity for Xe/Kr, limiting their practical applications [7].

As a new type of crystalline materials, metal-organic frameworks (MOFs) have emerged as promising adsorbents for gas separation due to their powerful predictability and tunability on pore environment (e.g. surface chemistry) and pore diameters [8–32]. These advanced features have allowed the pore size/shape in a customized MOF to match the target adsorbate molecules, enhancing the adsorption selectivity and capacity in the separation of CO_2/N_2 [33,34], C_2H_2/CO_2 [35–42], C_2H_2/C_2H_4 [43–46], C_2H_6/C_2H_4 [47–50], C_3H_4/C_3H_6 [51,52], C_3H_6/C_3H_8 [53], SO_2/CO_2 [54,55], *etc*. When compared, the Xe/Kr separation is more challenging and less explored [56–65]. Anion pillared MOFs (APMOFs) are a new class of MOFs with multi-nucleus inorganic anions (eg, SiF_6^{2-}, TiF_6^{2-}, $B_{12}H_{12}^{2-}$, CrO_4^{2-}, *etc*) decorated in the pore surface [66]. The reasonable combination of anion pillars and organic linkers endows this kind of materials superior performance in gas separation. For example, pillared-layered SIFSIX-14-Cu-i can adsorb acetylene strongly through the hydrogen bonding interaction between F atoms and acetylene H atoms while nearly completely blocking ethylene [67]. For another example, pillar-caged TIFSIX-Cu-TPA can efficiently capture CO_2 from flue gas with both extremely high CO_2/N_2 selectivity and high CO_2 capacity [34]. To date, the Xe/Kr separation has only been studied in pillar-layered APMOFs with high selectivity [68]. However, many of pillar-layered APMOFs display poor chemical stability, limiting its practical applications. In contrast, the recently reported pillar-caged APMOF TIFSIX-Cu-TPA is tolerant in dilute acid and base. Thus, we are motivated to investigate the Xe/Kr separation performance in pillar-caged APMOFs.

Herein, we reported the excellent Xe/Kr adsorption and separation performance in three isostructural fluorinated pillar-caged APMOFs, namely TIFSIX-Cu-TPA, GeFSIX-Cu-TPA and NbOFFIVE-Cu-TPA (A-Cu-TPA). Single component gas adsorption isotherms showed that TIFSIX-Cu-TPA, GeFSIX-Cu-TPA and NbOFFIVE-Cu-TPA all exhibit much higher uptakes of Xe than Kr at 298 K and 100 kPa. The Xe capacities at 298 K and 1.0 bar are 64.5, 61.2 and 59.0 STP $cm^3\ g^{-1}$respectively, while those for Kr are only 16.9, 15.8 and 14.9 STP $cm^3\ g^{-1}$. The IAST selectivities calculated by ideal adsorbed solution theory (IAST) are 5.4, 5.3 and 5.1 for Xe/Kr (20/80) at 298 K. The Xe/Kr binding sites were studied by Grand Canonical Monte Carlo (GCMC) simulations and density functional theory (DFT) calculations, indicating the preferable binding with Xe over Kr in the cages decorated with fluorine atoms, consistent with the experimental results. The dynamic Xe/Kr separation performance is further demonstrated by transient breakthrough simulations.

2. Experimental

Tri(pyridin-4-yl)amine (TPA, 99%), $Cu(NO_3)_2{\cdot}3H_2O$ (99%), $(NH_4)_2GeF_6$ (99.99%) and CuO (99%) were purchased from Energy Chemical. $(NH_4)_2TiF_6$ (98%) was purchased from Alab Chemical. Nb_2O_5 was purchased from Macklin. HF (≥40%) was purchased from Greagent. Xe (99.99%), Kr (99.99%), N_2 (99.9999%), He (99.9999%) and Ar (99.9999%) were purchased from Datong Co., Ltd.

2.1. Preparation of TIFSIX-Cu-TPA, GeFSIX-Cu-TPA and NbOFFIVE-Cu-TPA

Preparation of $CuNbOF_5{\cdot}4H_2O$: $CuNbOF_5{\cdot}4H_2O$ was prepared according to the reported literature [52]. CuO (1.50 g, 18.9 mmol, 2 eq), Nb_2O_5 (2.51 g, 9.45 mmol, 1 eq) and 4.11 mL HF (aq, 40%, 10 eq) were added to a 50 mL Teflon lined stainless autoclave. The mixture was stirred under the room temperature for 2 h and then was heated at 60 °C for 24 h. After that the mixture was cooled to room temperature and a clear blue aqueous $CuNbOF_5$ solution was obtained. After removing the solid by filtration, the blue aqueous solution was evaporated at 80 °C for more than 5 h in an oil bath, yielding the blue crystalline powder of $CuNbOF_5{\cdot}4H_2O$ (5.2 g, 81.0% based on CuO).

TIFSIX-Cu-TPA was prepared according to our previous work [69]. To a 5 mL long thin tube was added with $Cu(NO_3)_2{\cdot}3H_2O$ (~1.3 mg) and $(NH_4)_2TiF_6$ (~1.0 mg) in aqueous solution (1 mL). MeOH/H_2O mixture (v:v = 1:1, 2 mL) was slowly layered above the solution, followed by MeOH solution (1 mL) of TPA (~1.0 mg). The tube was sealed and left undisturbed at 298 K. After ~1 week, purple single crystals were obtained.

GeFSIX-Cu-TPA was prepared according to our previous work [20]. To a 5 mL long thin tube was added with $Cu(NO_3)_2{\cdot}3H_2O$ (~1.3 mg) and $(NH_4)_2GeF_6$ (~1.0 mg) in aqueous solution (1 mL). MeOH/H_2O mixture (v:v = 1:1, 2 mL) was slowly layered above the solution, followed by MeOH solution (1 mL) of TPA (~1.0 mg). The tube was sealed and left undisturbed at 298 K. After ~1 week, purple single crystals were obtained.

NbOFFIVE-Cu-TPA was prepared according to the our previous work [34]. To a 5 mL long thin tube was added with $CuNbOF_5{\cdot}4H_2O$ (~1.8 mg) in aqueous solution (1 mL). MeOH/H_2O mixture (v:v = 1:1, 2 mL) was slowly layered above the solution, followed by MeOH solution (1 mL) of TPA (~1.0 mg). The tube was sealed and left undisturbed at 298 K. After ~1 week, purple single crystals were obtained.

2.2. Gas adsorption isotherms measurements

The gas adsorption isotherms measurements were performed on a Builder SSA 7000 (Beijing) instrument with two separated stations. Before gas adsorption measurements, the samples were evacuated at 25 °C for 2 h firstly, and then at 120 °C for 10 h until the pressure dropped below 0.1 Pa.

2.3. Fitting of pure component isotherms

The adsorption isotherms in A-Cu-TPA (A = TIFSIX, GeFSIX and NbOFFIVE) were fitted using a single-site Langmuir model:

$$q = q_{sat}\frac{bp}{1+bp} \tag{1a}$$

P is the pressure of the bulk gas at equilibrium with the adsorbed phase (kPa), q is the adsorbed amount per mass of adsorbent (mol kg^{-1}), b is the affinity coefficients (Pa^{-1}) and temperature dependent.

$$b = b_o\, e^{E/(RT)} \tag{1b}$$

E is the energy parameter (kJ/mol).

All the adsorption isotherms are fitted with excellent accuracy ($R^2 > 0.999$). The single-site Langmuir parameter fits for gases in A-Cu-TPA are shown in Table 1.

The isosteric heat of adsorption, Q_{st}, is defined as

$$Q_{st} = -RT^2\left(\frac{\partial \ln p}{\partial T}\right)_q \tag{2}$$

The derivative in the right member of eq (2) is determined at constant adsorbate loading, q (mol kg^{-1}). The calculations are based on the use of the Clausius-Clapeyron equation.

Table 1
Single-site Langmuir parameter fits.

MOFs	Gas	Adsorbed amount q_{sat} (mol kg^{-1})	Equilibrium constant b (Pa^{-1})	Energy parameter E (kJ/mol)
TIFSIX-Cu-TPA	Xe	8	6.639E-10	22.3
	Kr	8	8.521E-10	17.5
GeFSIX-Cu-TPA	Xe	8.2	7.593E-10	21.7
	Kr	8.2	6.649E-10	17.9
NbOFFIVE-Cu-TPA	Xe	9.2	6.498E-10	21.5
	Kr	6.2	9.112E-10	17.7

The IAST adsorption selectivity for two gases is defined as:

$$S_{ads} = \frac{q_1/q_2}{y_{10}/y_{20}} \quad (3)$$

Here, q_1, and q_2 are the loadings in the adsorbed phase in equilibrium. y_{10}, y_{20} are the mole fractions of the bulk gas phase mixture.

2.4. Transient breakthrough simulations

Transient breakthrough simulations were carried out for binary 20/80 Xe(1)/Kr(2) mixtures at three different temperatures 278 K, and 298 K and 308 K in TIFSIX-Cu-TPA, GeFSIX-Cu-TPA, and NbOFFIVE-Cu-TPA under a total pressure of 100 kPa. In these simulations, intra-crystalline diffusion influences are ignored. These simulations were performed in a bed with the following parameters: adsorber length, $L = 0.3$ m; cross-sectional area, $A = 1$ m^2; interstitial gas velocity in the bed, $v = 0.1$ m s^{-1}; voidage of the packed bed, $= 0.4$; the superficial gas velocity at the inlet to the bed, $u_0 = 0.04$ m s^{-1}. The volume of zeolite or MOF used in the simulations is $V_{ads} = LA(1 - \varepsilon) = 0.18$ m^3. Also, note that since the superficial gas velocity is specified, the specification of the cross-sectional area of the tube, A, is not relevant in the simulation results presented; essentially, we set $A = 1$ m^2. The total volume of the bed is $V_{bed} = LA$. It is important to note that the volume of adsorbent, V_{ads}, includes the pore volume of the adsorbent material. If ρ is the framework density, the mass of the adsorbent in the bed is $m_{ads} = (1 - \varepsilon) \times (L \text{ m}) \times (A\text{m}^2) \times (\rho \text{kg m}^{-3})$ kg. In these breakthrough simulations we use the same volume of adsorbent in the breakthrough apparatus, i.e. $(1 - \varepsilon) \times A \times L = 0.18$ m$^3 = 180$ L.

The breakthrough data are presented in terms of the dimensionless concentrations at the exit of the fixed bed, c_i/c_{i0}, as function of the modified time parameter $\frac{(Q_0=\text{flow rate L s}^{-1}) \times (\text{time in s})}{(\text{kg MOF packed in tube})} = \frac{Q_0 t}{m_{ads}} = \text{L kg}^{-1}$.

2.5. Breakthrough experiments

The breakthrough experiments were carried out in the dynamic gas breakthrough equipment HP-MC41. The experiments were conducted using a stainless steel column (4.9 mm inner diameter × 50 mm length). The weight of TIFSIX-Cu-TPA packed in the columns was 0.51 g. The column packed with sample was first purged with a Ar flow (5 mL min^{-1}) for 18 h at ~120 °C. The mixed gas of Xe/Kr (v/v, 20:80) was then introduced. The working temperature is ~20 °C. Outlet gas from the column was monitored using gas chromatography (GC-9860-5CNJ) with the thermal conductivity detector TCD.

2.6. Grand canonical Monte Carlo (GCMC) simulations

Grand canonical Monte Carlo (GCMC) simulations were performed in RASPA package. The structure of TIFSIX-Cu-TPA was firstly optimized via DFT geometry optimization (see detailed protocol below). Because both Xe and Kr atoms are charge neutral, no Coulomb interaction was calculated. For the van der Waals interaction, Lennard-Jones parameters for all aromatic C, H, N were taken from OPLS-AA force field, while parameters for the rest atoms were taken from the universal force field (UFF). Krypton (Kr) and xenon (Xe) were modeled as single spheres. The framework was considered to be rigid during the simulation and the interaction energy between the adsorbed molecules and the framework were computed through the Lennard-Jones 6–12 (LJ) potentials. The cutoff radius was chosen 12.8 Å for the van der Walls interaction. For each applied pressure, we carried out 40,000 cycles of Monte Carlo moves including insertion, deletion, translation, rotation, and reinsertion. Because both Kr and Xe atoms are charge neutral, we did not assign charges to MOF atoms and thus only van der Waals interactions were calculated.

2.7. DFT calculation

All first-principle calculations were performed within the framework of the spin-polarized density functional theory (DFT) as implemented in the VASP package. The Perdew-Burke-Ernzerhof (PBE) of Generalized Gradient Approximation (GGA) functional and Projection Augmented Wave (PAW) method were used to describe the exchange-correlation interaction and electron-ion interaction, respectively. The PBE-D3 method with Beck Johnson damping and Hubbard U correction was used for geometry optimization and U value was set to 4.0 eV. In all calculations, the plane wave cut-off energy was set to 520 eV, and the convergences of energy and force were 10^{-5} eV and 0.05 eV/Å, respectively. For geometry optimization, the k-point grids sampled in Brillouin zones were 3 × 3 × 1. The binding energy (ΔE) can be obtained from the equation: ΔE = E (MOF + gas) – [E (MOF) + E (gas)].

3. Results and discussion

Single crystals of A-Cu-TPA (A = TIFSIX, GeFSIX and NbOFFIVE) were all cultivated by layering a MeOH solution of TPA onto an aqueous solution of metal salts ($CuTiF_6$, $CuGeF_6$ or $CuNbOF_5$) (Fig. 1a and b) [34]. Single-crystal X-ray diffraction analysis indicated that the three MOFs are isomorphic and crystallize under a highly symmetric three-dimensional space group framework. The structure comparison of A-Cu-TPA is presented in Table S1. The framework consists of large icosahedral cages (~8.5 Å, Fig. 1c) and small tetrahedral cages (~4 Å, Fig. 1d), which are connected to each other through contracted windows. The large icosahedral cage contains six anions and the small tetrahedral cage contains two anions. Therefore, there are abundant of Lewis basic F functional sites in the pore surface for gas adsorption.

The PXRD patterns for the as-synthesized samples matches well with those calculated from single crystal structures, indicating that A-Cu-TPA MOFs were successfully synthesized with high purity (Fig. 1e and S1, 2). Notably, all the three MOFs maintained their crystallinity after being heated at 120 °C and in dynamic vacuum for 24 h. TIFSIX-Cu-TPA remains stable even after being soaked in water, DMF and dilute HCl (aq) solutions or exposed to a moist HCl vapor at 50 °C. The Thermogravimetric analyses (TGA) curves reveal that the three materials have good thermal stability. Particularly, NbOFFIVE-Cu-TPA and TIFSIX-Cu-TPA are stable over 300 °C (Fig. 1f).

The permanent porosity of A-Cu-TPA (A = TIFSIX, GeFSIX and NbOFFIVE) were confirmed by N_2 adsorption at 77 K. Before N_2 adsorption measurements, these samples were activated at 120 °C under vacuum for 12 h. All the N_2 adsorption isotherms exhibited a typical type-I adsorption profile. The BET surface areas calculated from 77 K N_2 gas adsorption experiments (Figs. S3–5) were as follows: 1380 m^2/g for TIFSIX-Cu-TPA, 1330 m^2/g for GeFSIX-Cu-TPA, and 1281 m^2/g for NbOFFIVE-Cu-TPA.

Next, we investigated the potential of selective Xe/Kr adsorption in these three APMOFs. Xe and Kr adsorption isotherms at 278, 298 and 308 K were all collected (Fig. 2a–c). As shown in Fig. 2a, Xe isotherms in the three APMOFs are similar while TIFSIX-Cu-TPA displays slightly higher adsorption capacity of 64.5 cm^3 g^{-1} at 298 K and 1 bar. Under the same conditions, the uptakes of Xe for GeFSIX-Cu-TPA and NbOFFIVE-Cu-TPA are 61.2 and 59.0 cm^3 g^{-1}, respectively. At 278 K and 1 bar, the Xe uptakes of all three APMOFs are increased to 93.2, 87.8 and 87.3 cm^3 g^{-1}, respectively (Fig. 2b). The same order for capacity is also observed at 308 K (Fig. 2c). The adsorption capacity decreases along with the temperature increase, which is a typical feature of physical adsorption. When compared, the saturated adsorption capacities of Kr are significantly lower. For TIFSIX-Cu-TPA, the saturated adsorption capacities are 25.8, 16.9 and 13.5 cm^3 g^{-1} at 278, 298 and 308 K, respectively (Fig. 2d–f). For all three APMOFs, the adsorption capacities of Xe are nearly 4 folds of those of Kr at 298 K and 1 bar, which can be explained by the fact that Xe has higher polarizability and larger molecular size than Kr and can interact with the polar APMOF surface more

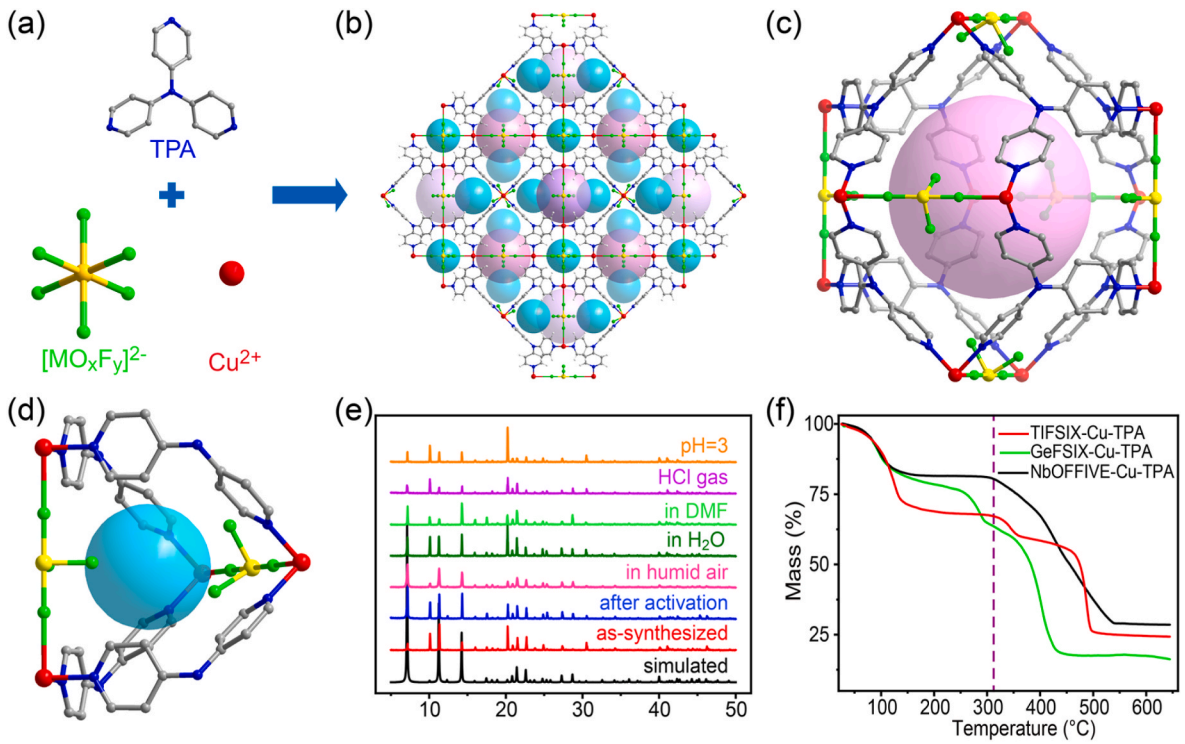

Fig. 1. (a) Basic units to construct A-Cu-TPA (A = TIFSIX, GeFSIX and NbOFFIVE). (b) Overview of the porous structure of A-Cu-TPA; (c) The large cage of TIFSIX-Cu-TPA; (d) The small cage of TIFSIX-Cu-TPA; (e) PXRD of TIFSIX-Cu-TPA after different treatment; (f) TGA curves of TIFSIX-Cu-TPA, GeFSIX-Cu-TPA and NbOFFIVE-Cu-TPA.

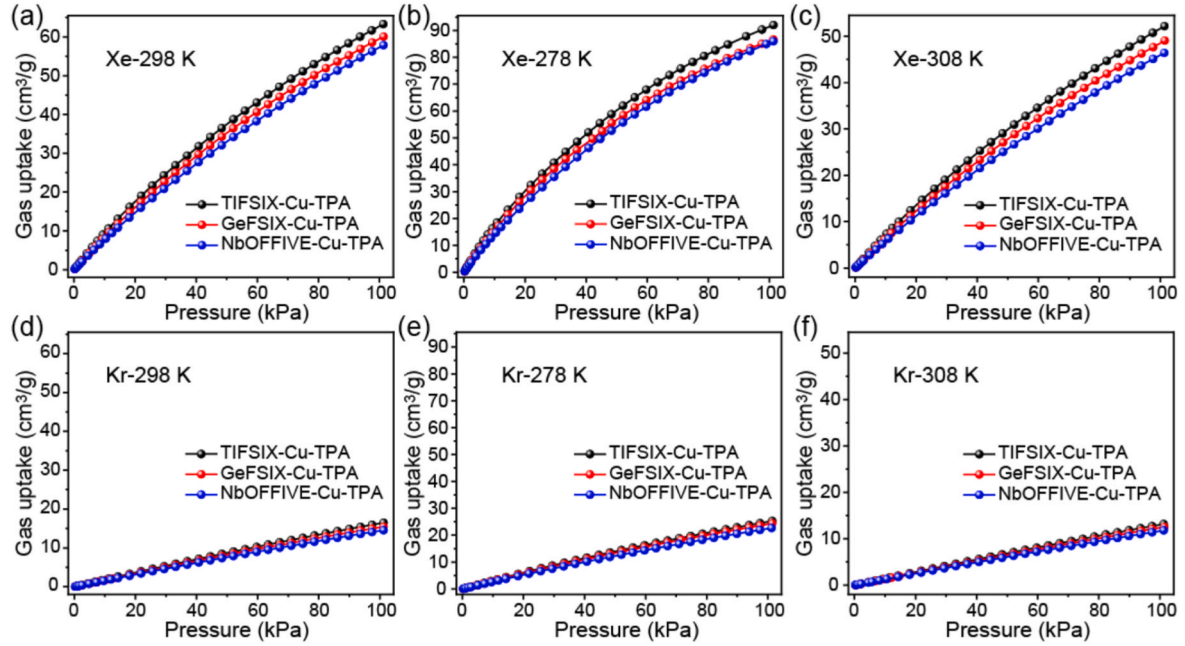

Fig. 2. The adsorption equilibrium of Xe and Kr on A-Cu-TPA (A = TIFSIX, GeFSIX and NbOFFIVE) at 278–308 K.

strongly.

To further compare A-Cu-TPA (A = TIFSIX, GeFSIX and NbOFFIVE), the separation selectivities for Xe/Kr gas mixtures were calculated using ideal adsorbed solution theory (IAST) after fitting the adsorption isotherms to single-site Langmuir equations (Table 1). The ratio was selected according to the typical composition of real industrial Xe/Kr mixtures. The calculated IAST selectivities of Xe/Kr (20/80) are 5.4 (TIFSIX-Cu-TPA), 5.3 (GeFSIX-Cu-TPA) and 5.1 (NbOFFIVE-Cu-TPA) at 100 kPa and 298 K (Fig. 3a–c), respectively. The selectivities increase along with the pressure, which can be attributed to the stronger guest-guest interaction for Xe with larger atomic size. The Xe/Kr IAST selectivity value of TIFSIX-Cu-TPA is higher than those of some reported MOFs including SIFSIX-3-Cu [68], MFU-4l [70], NU-403 [71], *etc*, but lower than those of UTSA-74 [72], CPM-6 [73], MOF-505 [74], *etc* (Fig. 3d). In addition, the selectivity of Xe/Kr (20/80) increases with the decrease of temperature. The IAST selectivities of Xe/Kr for

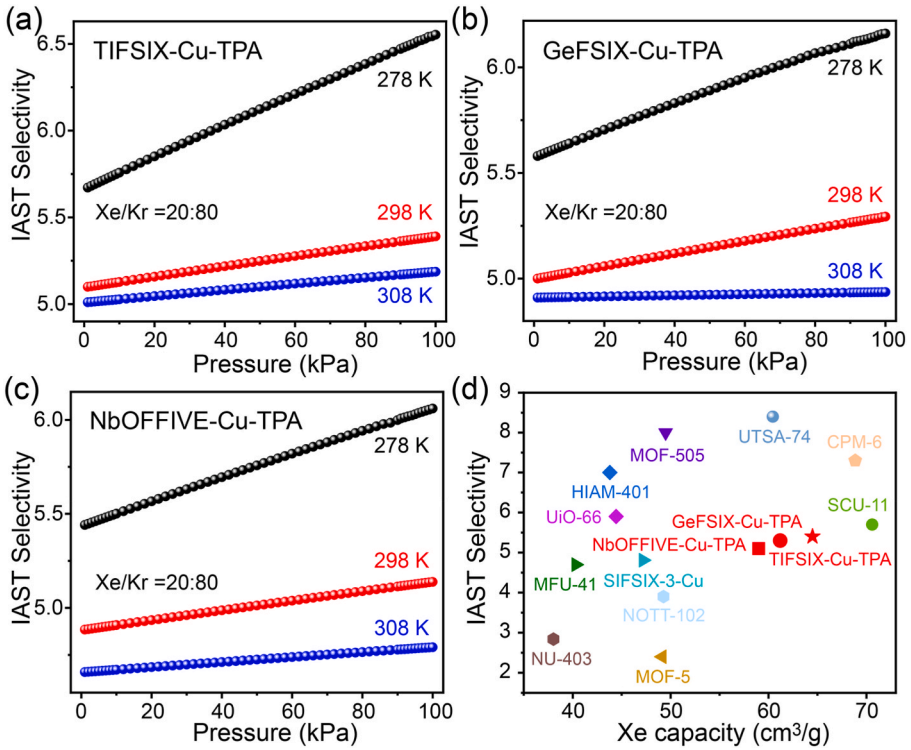

Fig. 3. (a) IAST selectivity of Xe/Kr (20/80) in TIFSIX-Cu-TPA; (a) IAST selectivity of Xe/Kr (20/80) in GeFSIX-Cu-TPA; (c) IAST selectivity of Xe/Kr (20/80) in NbOFFIVE-Cu-TPA; (d) comparison of the IAST selectivity and Xe capacity at 1.0 bar among popular MOFs.

TIFSIX-Cu-TPA, GeFSIX-Cu-TPA and NbOFFIVE-Cu-TPA at 278 K are 6.5, 6.3 and 6.1, respectively (Fig. 3a–c). Under all the temperatures, the IAST selectivities increase with the total pressure. This is probably due to the stronger guest-guest interaction for Xe in these APMOFs.

The isosteric adsorption enthalpy (Q_{st}) is another important parameter to evaluate the MOF's affinity towards adsorbate. Higher Q_{st} means stronger host-guest interaction and higher selectivity in most cases. However, it also indicates the increased energy footprint to regenerate

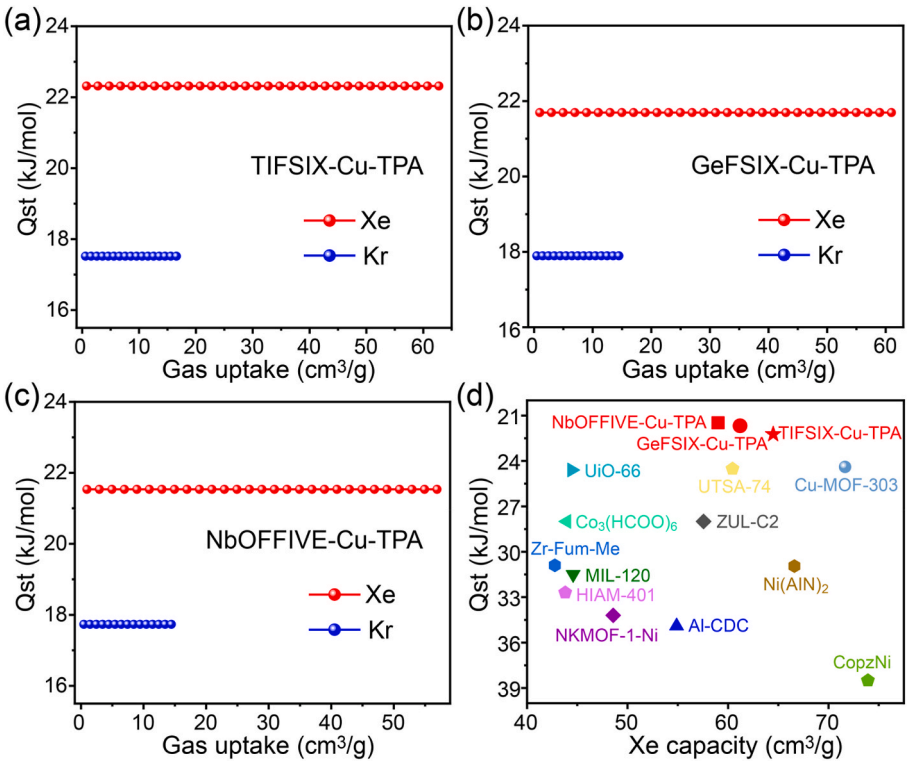

Fig. 4. (a) Q_{st} curve of Xe and Kr adsorption in TIFSIX-Cu-TPA; (b) Q_{st} curve of Xe and Kr adsorption in GeFSIX-Cu-TPA; (c) Q_{st} curve of Xe and Kr adsorption in NbOFFIVE-Cu-TPA; (d) comparison of the near-zero loading Q_{st} of Xe and Xe capacity at 1.0 bar.

the material. Thus, modest high Q_{st} is preferred considering both the adsorption and desorption process. As shown in Fig. 4a–c, Q_{st} values at near-zero loading for Xe (Kr) calculated using the Clausius-Clapeyron equation were 22.3 kJ/mol for TIFSIX-Cu-TPA, 21.7 kJ/mol for GeFSIX-Cu-TPA, and 21.5 kJ/mol for NbOFFIVE-Cu-TPA, respectively, while those for Kr are 17.5, 17.9, and 17.7 kJ/mol. These results are in line with the relatively flat Xe and Kr adsorption isotherms as well as the higher Xe adsorption affinity. Notably, these Q_{st} values for Xe adsorption are also much lower than those of many MOFs such as UiO-66 [75], Cu-MOF-303 [76], ZUL-C2 [77], MIL-120 [78], HIAM-401 [79], NKMOF-1-Ni [80], Al-CDC [65], *etc* (Fig. 4d and Table S3), indicating these three APMOFs can be regenerated under mild condition.

To gain insights into the adsorption behaviors of Xe and Kr in TIFSIX-Cu-TPA, GCMC simulations were performed. First, the comparison of experimental and simulated adsorption isotherms (Fig. 5a) suggests that our GCMC results are close to the experimental results while the simulated Xe isotherms show slight lower uptake, which is yet still reasonable and indicates that our GCMC simulation with calibrated force fields for TIFSIX-Cu-TPA can almost reflect the adsorption behavior of Xe and Kr in the TIFSIX-Cu-TPA. GCMC simulation shows that Xe only contains a binding site in the large cage (Fig. 5b), while Kr owns two different binding sites: one is located in the large cage, and the other is located in the small cage (Fig. 5c). Then, DFT calculations were performed to obtain the binding energies of Xe in TIFSIX-Cu-TPA. As shown in Fig. 5d, the Xe atom interacts with two F atoms at the edges of cages at distances of 3.98 Å and 3.99 Å, respectively. In addition, it also interacts with four hydrogen atoms of the pyridine ring at the distances of 3.68–3.86 Å. All of these interactions produce a modestly high binding energy of −0.44 eV (−42.5 kJ/mol). For Kr in TIFSIX-Cu-TPA, the adsorption sites in large cages were formed between Kr and F atoms or H atoms from pyridine ring with distances of 2.30–3.27 Å (Fig. 5e). The resulting adsorption energy is −0.40 eV (−38.6 kJ/mol). In the small cages, the distances between Kr···H and Kr···F are 2.94–3.94 Å (Fig. 5f) and the binding energy is as low as −0.15 eV (−14.5 kJ/mol). This is quite different from CO_2 or light hydrocarbon adsorption [20,34] where the small cages are the preferable binding sites. Besides, it is necessary to mention that the binding energy, instead of the interaction distance, should be the indicator of the strength of host-guest interactions. In this case, Xe-framework distance is longer than Kr-framework distance because Xe has larger atomic size. Similar phenomenon of longer interaction distance but stronger binding energy has ever been reported in our previous work for C_3H_4/C_3H_6 separation [52]. In brief, DFT calculation results show that Xe interacts with TIFSIX-Cu-TPA more strongly than Kr, consistent with the experimental findings.

To evaluate the feasibility of A-Cu-TPA (A = TIFSIX, GeFSIX and NbOFFIVE) for practical dynamic Xe/Kr separation, transient breakthrough simulations of Xe/Kr (20/80) mixture were conducted at 278, 298 and 308 K. The methodology used in the simulations were well developed in the earlier works of Krishna [81,82] and has shown high consistency with the experimental breakthrough curves under the same conditions [14,69]. As shown in Fig. 6, for all the three materials under three different temperatures, the Kr breakthrough occurs first and subsequently reaches a plateau while the Xe breakthrough time is significantly longer, confirming the effective Xe/Kr separation performance. The calculated productivities of pure Kr are 75.1, 41.1 and 30.7 L/kg for TIFSIX-Cu-TPA at 278, 298 and 308 K, respectively. For GeFSIX-Cu-TPA and NbOFFIVE-Cu-TPA, the productivities of pure Kr are slightly decreased to 68.1/38.0/28.6 L/kg and 60.5/33.3/25.1 L/kg under the same conditions. These productivities are superior to those of many popular MOFs in the context of Xe/Kr separation [72].

To confirm the practical Xe/Kr separation performance of these pillar-caged MOFs, TIFSIX-Cu-TPA was selected as the candidate for the Xe/Kr breakthrough experiments. A mixture of Xe/Kr (20/80) was introduced into a column packed with 0.51 g of TIFSIX-Cu-TPA and the outlet concentration was monitored consistently. As expected, Kr broke out from the column fixed bed at the beginning while Xe stayed for a

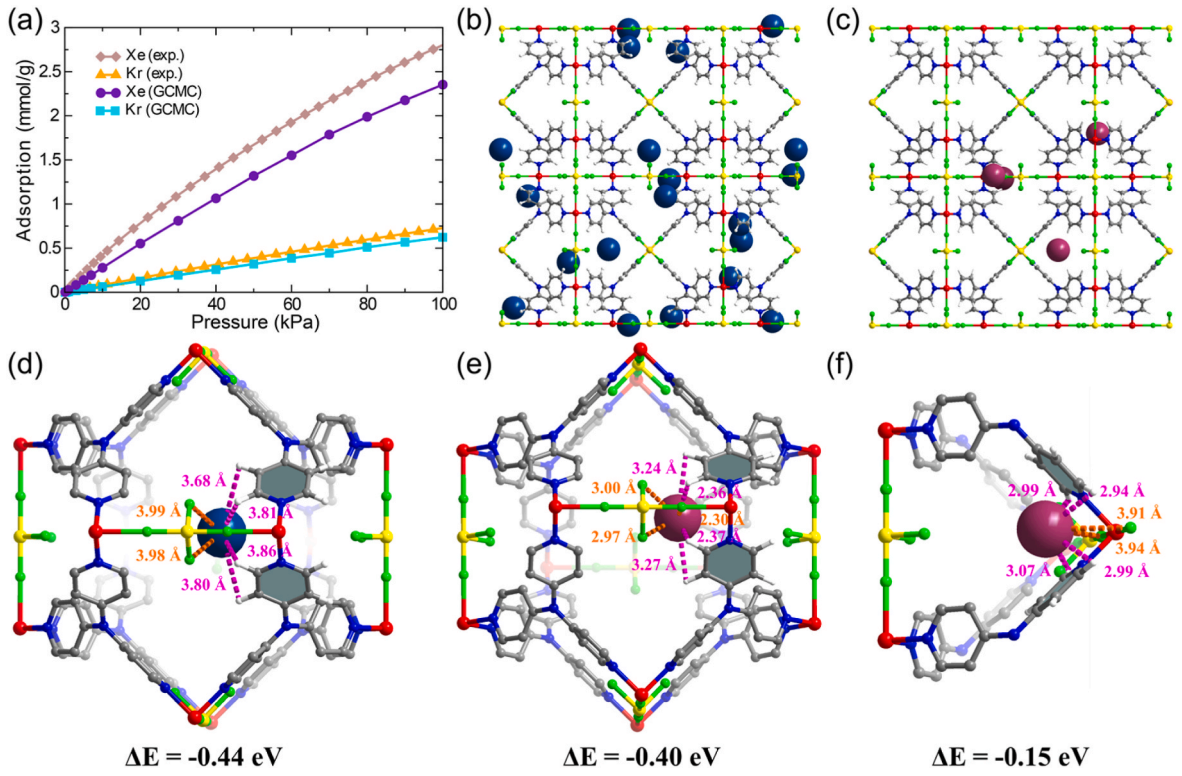

Fig. 5. (a) Comparison of the experimental and simulated adsorption isotherms of Xe and Kr in TIFSIX-Cu-TPA at 298 K; (b) A snapshot of Xe-loaded TIFSIX-Cu-TPA structure from GCMC simulation results; (c) A snapshot of Kr-loaded TIFSIX-Cu-TPA structure from GCMC simulation results; (d) DFT optimized Xe adsorption site in TIFSIX-Cu-TPA; (e, f) Two DFT optimized Kr adsorption sites in TIFSIX-Cu-TPA.

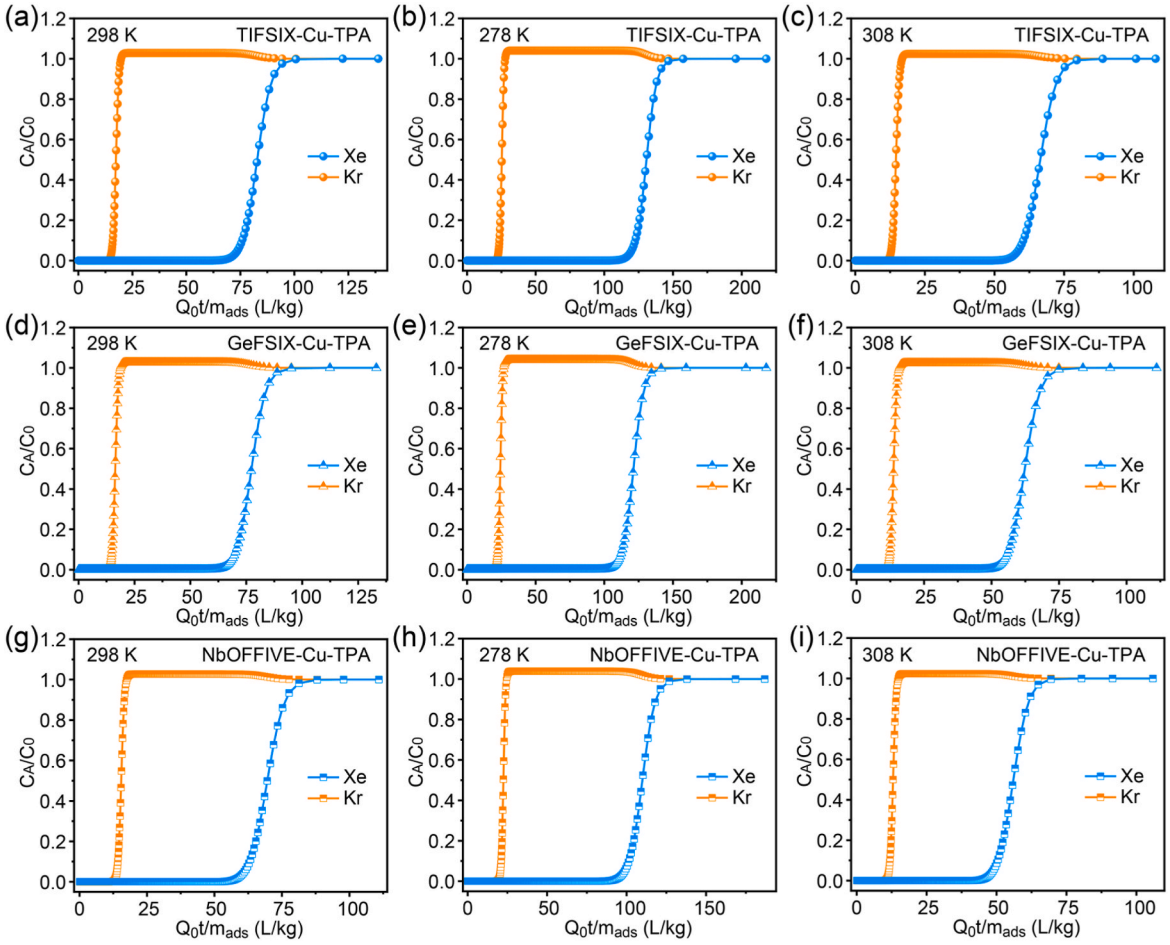

Fig. 6. (a–c) Simulated breakthrough curves for Xe/Kr (20/80) separation on TIFSIX-Cu-TPA at 278–308 K; (d–e) Simulated breakthrough curves for Xe/Kr (20/80) separation on GeFSIX-Cu-TPA at 278–308 K; (g–i) Simulated breakthrough curves for Xe/Kr (20/80) separation on NbOFFIVE-Cu-TPA at 278–308 K.

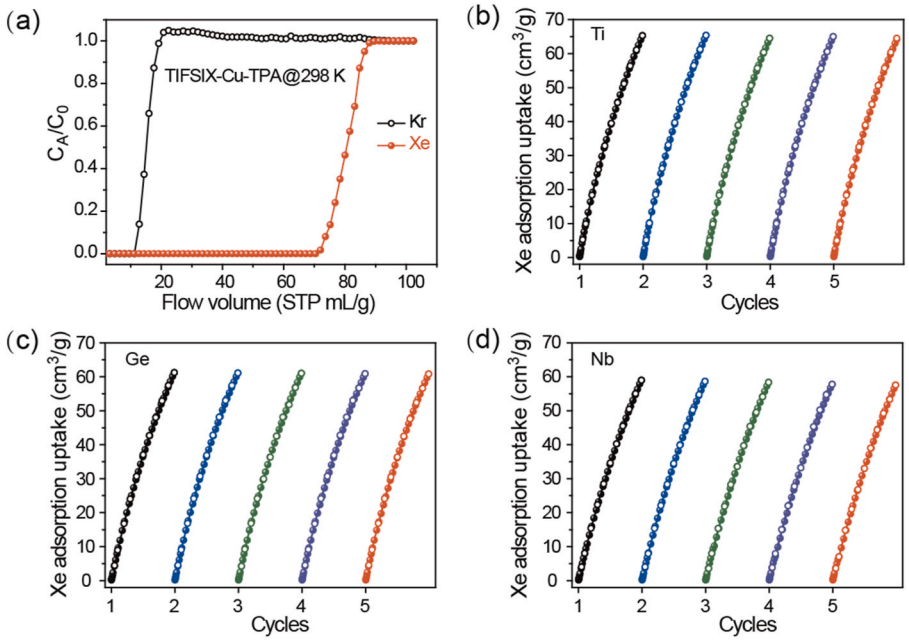

Fig. 7. (a) Experimental breakthrough curves for Xe/Kr (20/80) separation on TIFSIX-Cu-TPA; (b–d) repetitive Xe adsorption isotherms at 298 K for TIFSIX-Cu-TPA, GeFSIX-Cu-TPA and NbOFFIVE-Cu-TPA under different treatment: generated at 120 °C for 0.5 h (blue); generated at 25 °C for 2 h (olive); in humid air for over 1 month (violet); in water for over 1 month (red).

much longer period (Fig. 7a), which is quite similar to the simulation results. The experimental Kr productivity is 42.6 mL/g, consistent with the simulated results. To explore the recyclable stability and the regeneration conditions, repetitive Xe and Kr adsorption isotherms were collected for all the three APMOFs (Fig. 7b–d), which shows that these APMOFs can be readily regenerated at room temperature under dynamic vacuum and retain the same adsorption capacity. This is consistent with the low adsorption heats of Xe in these APMOFs. Moreover, the Xe capacity can be sustained after the samples are soaked in water for over one month, which is also confirmed by the repetitive N_2 adsorption isotherms at 77 K (Figs. S12–14).

4. Conclusion

In conclusion, we reported three water stable APMOFs, TIFSIX-Cu-TPA, GeFSIX-Cu-TPA and NbOFFIVE-Cu-TPA, for the efficient Xe/Kr separation. Among them, TIFSIX-Cu-TPA shows the best separation performance of Xe/Kr, with its Xe adsorption capacity of 64.5 $cm^3\ g^{-1}$ at 298 K and 1 bar, good Xe/Kr (20/80) IAST selectivity (5.4), moderate adsorption heat (22.3 kJ/mol). GCMC simulations yield similar results with experimental ones and reveal several adsorption sites for Xe/Kr. DFT calculations further demonstrate that Xe possesses a stronger binding to TIFSIX-Cu-TPA than Kr through multiple interactions with neighboring atoms such as Xe···F and Xe···H. Transient breakthrough simulations and experiments confirm the effective separation performance of TIFSIX-Cu-TPA in separating Xe/Kr gas mixture. These fluorinated pillared caged APMOFs can potentially overcome the difficulties of Xe/Kr separation in industrial processes, owing to their balanced capacity and selectivity, excellent chemical stability and low adsorption heats.

CRediT authorship contribution statement

Jiahao Li: Investigation. **Lingyao Wang:** Investigation. **Yuxin Chen:** Investigation. **Zonglin Gu:** Methodology, Investigation. **Tao Jiang:** Investigation. **Binquan Luan:** Investigation. **Rajamani Krishna:** Investigation. **Yuanbin Zhang:** Conceptualization.

Declaration of competing interest

The authors declare that they have no conflicts of interest to this work.

Data availability

Data will be made available on request.

Acknowledgement

Yuanbin Zhang acknowledges the support of Jinhua Industrial Key Project (No. 2021-1-088) and financial support by Open Research Fund of Key Laboratory of the Ministry of Education for Advanced Catalysis Materials and Zhejiang Key Laboratory for Reactive Chemistry on Solid Surfaces, Zhejiang Normal University (No. KLMEACM202211). Lingyao Wang acknowledges the support of Natural Science Foundation of China (No. 22205207). Zonglin Gu acknowledges the support of National Natural Science Foundation of China (No. 12104394), Natural Science Research of Jiangsu Higher Education Institutions of China (No. 21KJB140024) and the Youth Hundred Talents Program of Yangzhou University.

Appendix A. Supplementary data

Supplementary data to this article can be found online at https://doi.org/10.1016/j.micromeso.2023.112631.

References

[1] G.A. Lane, M.L. Nahrwold, A.R. Tait, M. Taylor-busch, P.J. Cohen, A.R. Beaudoin, Anesthetics as teratogens: nitrous oxide is fetotoxic, xenon is not, Science 210 (1980) 899–901.
[2] J. Marshall, A.C. Bird, A comparative histopathological study of argon and krypton laser irradiations of the human retina, Br. J. Ophthalmol. 63 (1979) 657–668.
[3] F. Chen, J. Ding, K. Guo, L. Yang, Z. Zhang, Q. Yang, Y. Yang, Z. Bao, Y. He, Q. Ren, CoNi alloy nanoparticles embedded in metal-organic framework-derived carbon for the highly efficient separation of xenon and krypton via a charge-transfer effect, Angew. Chem. Int. Ed. 60 (2021) 2431–2438.
[4] L.T. Liu, Y. Xu, P. Tang, Mechanistic insights into xenon inhibition of NMDA receptors from MD simulations, J. Phys. Chem. B 114 (2010) 9010–9016.
[5] F.G. Kerry, Industrial Gas Handbook: Gas Separation and Purification, CRC Press, Boca Raton, LA, 2007.
[6] H. Zhang, Y. Fan, R. Krishna, X. Feng, L. Wang, F. Luo, Robust metal-organic framework with multiple traps for trace Xe/Kr separation, Sci. Bull. 66 (2021) 1073–1079.
[7] R.E. Bazan, M. Bastos-Neto, A. Moeller, F. Dreisbach, R. Staudt, Adsorption equilibria of O_2, Ar, Kr and Xe on activated carbon and zeolites: single component and mixture data, Adsorption 17 (2011) 371–383.
[8] L. Zhang, K. Jiang, L. Yang, L. Li, E. Hu, L. Yang, K. Shao, H. Xing, Y. Cui, Y. Yang, B. Li, B. Chen, G. Qian, Benchmark C_2H_2/CO_2 separation in an ultra-microporous metal-organic framework via copper(I)-Alkynyl chemistry, Angew. Chem. Int. Ed. 60 (2021) 15995–16002.
[9] H. Zeng, X.-J. Xie, M. Xie, Y.-L. Huang, D. Luo, T. Wang, Y. Zhao, W. Lu, D. Li, Cage-interconnected metal-organic framework with tailored apertures for efficient C_2H_6/C_2H_4 separation under humid conditions, J. Am. Chem. Soc. 141 (2019) 20390–20396.
[10] N. Xu, J. Hu, L. Wang, D. Luo, Y. Hu, D. Wang, X. Cui, H. Xing, Y. Zhang, A TIFSIX pillared MOF with unprecedented zsd topology for efficient separation of acetylene from quaternary mixtures, Chem. Eng. J. 450 (2022), 138034.
[11] G.-P. Li, Z.-Z. Li, H.-F. Xie, Y.-L. Fu, Y.-Y. Wang, Efficient C_2 hydrocarbons and CO_2 adsorption and separation in a multi-site functionalized MOF, Chin. J. Struct. Chem. 40 (2021) 1047–1054.
[12] W. Sun, J. Hu, Y. Jiang, N. Xu, L. Wang, J. Li, Y. Hu, S. Duttwyler, Y. Zhang, Flexible molecular sieving of C_2H_2 from CO_2 by a new cost-effective metal organic framework with intrinsic hydrogen bonds, Chem. Eng. J. 439 (2022), 135745.
[13] Z. Bao, D. Xie, G. Chang, H. Wu, L. Li, W. Zhou, H. Wang, Z. Zhang, H. Xing, Q. Yang, M.J. Zaworotko, Q. Ren, B. Chen, Fine tuning and specific binding sites with a porous hydrogen-bonded metal-complex framework for gas selective separations, J. Am. Chem. Soc. 140 (2018) 4596–4603.
[14] L. Wang, W. Sun, Y. Zhang, N. Xu, R. Krishna, J. Hu, Y. Jiang, Y. He, H. Xing, Interpenetration symmetry control within ultramicroporous robust boron cluster hybrid MOFs for benchmark purification of acetylene from carbon dioxide, Angew. Chem. Int. Ed. 60 (2021) 22865–22870.
[15] W. Sun, J. Hu, S. Duttwyler, L. Wang, R. Krishna, Y. Zhang, Highly selective gas separation by two isostructural boron cluster pillared MOFs, Sep. Purif. Technol. 283 (2022), 120220.
[16] L. Yu, X. Dong, Q. Gong, S.R. Acharya, Y. Lin, H. Wang, Y. Han, T. Thonhauser, J. Li, Splitting mono- and dibranched alkane isomers by a robust aluminum-based metal-organic framework material with optimal pore dimensions, J. Am. Chem. Soc. 142 (2020) 6925–6929.
[17] H. Fang, B. Zheng, Z.-H. Zhang, H.-X. Li, D.-X. Xue, J. Bai, Ligand-conformer-induced formation of zirconium-organic framework for methane storage and MTO product separation, Angew. Chem. Int. Ed. 60 (2021) 16521–16528.
[18] Y. Zhang, L. Yang, L. Wang, X. Cui, H. Xing, Pillar iodination in functional boron cage hybrid supramolecular frameworks for high performance separation of light hydrocarbons, J. Mater. Chem. 7 (2019) 27560–27566.
[19] M. Chang, J. Ren, Q. Yang, D. Liu, A robust calcium-based microporous metal-organic framework for efficient CH_4/N_2 separation, Chem. Eng. J. 408 (2021), 127294.
[20] Y. Jiang, Y. Hu, B. Luan, L. Wang, R. Krishna, H. Ni, X. Hu, Y. Zhang, Benchmark single-step ethylene purification from ternary mixtures by a customized fluorinated anion-embedded MOF, Nat. Commun. 14 (2023) 401.
[21] G. Li, G. Ji, X. Wang, W. Liu, D. Zhang, L. Chen, L. He, S. Liang, X. Li, F. Ma, S. Wang, Efficient and selective capture of xenon over krypton by a window-cage metal-organic framework with parallel aromatic rings, Sep. Purif. Technol. 295 (2022), 121281.
[22] W. Zhang, Y. Li, S. Wang, Y. Wu, S. Chen, Y. Fu, W. Ma, Z. Zhang, H. Ma, Fluorine-induced electric field gradient in 3D porous aromatic frameworks for highly efficient capture of Xe and F-gases, ACS Appl. Mater. Interfaces 14 (2022) 35126–35137.
[23] M. Kang, J.H. Choe, H. Kim, H. Yun, D.W. Kima, C.S. Hong, Ultramicroporous hydrogen-bond decorated robust metal-organic framework for high xenon capture performances Check for updates, J. Mater. Chem. 10 (2022) 24824–24830.
[24] Y. Zhang, X. Cui, H. Xing, Recent advances in the capture and abatement of toxic gases and vapors by metal-organic frameworks, Mater. Chem. Front. 5 (2021) 5970–6013.
[25] Y. Zhang, L. Yang, L. Wang, S. Duttwyler, H. Xing, A microporous metal-organic framework supramolecularly assembled from a Cu(II) dodecaborate cluster complex for selective gas separation, Angew. Chem. Int. Ed. 58 (2019) 8145–8150.
[26] P. Hu, J. Hu, H. Wang, H. Liu, J. Zhou, Y. Liu, Y. Wang, H. Ji, One-Step ethylene purification by an ethane-screening metal-organic framework, ACS Appl. Mater. Interfaces 14 (2022) 15195–15204.

[27] L. Gong, Y. Liu, J. Ren, A.M. Al-Enizi, A. Nafady, Y. Ye, Z. Bao, S. Ma, Utilization of cationic microporous metal-organic framework for efficient Xe/Kr separation, Nano Res. 15 (2022) 7559–7564.

[28] H. Yang, T. Trieu, X. Zhao, Y. Wang, Y. Wang, P. Feng, X. Bu, Lock and Key and shape-memory effects in an unconventional synthetic path to magnesium metal-organic frameworks, Angew. Chem. Int. Ed. 58 (2019) 11757–11762.

[29] G.-D. Wang, R. Krishna, Y.-Z. Li, W.-J. Shi, L. Hou, Y.-Y. Wang, Z. Zhu, Boosting ethane/ethylene separation by MOFs through the amino-functionalization of pores, Angew. Chem. Int. Ed. 61 (2022), e202213015.

[30] T. Li, X. Jia, H. Chen, Z. Chang, L. Li, Y. Wang, J. Li, Tuning the pore environment of MOFs toward efficient CH_4/N_2 separation under humid conditions, ACS Appl. Mater. Interfaces 14 (2022) 15830–15839.

[31] W. Zhang, Y. Li, Y. Wu, Y. Fu, S. Chen, Z. Zhang, S. He, T. Yan, H. Ma, Fluorinated porous organic polymers for efficient recovery perfluorinated electronic specialty gas from exhaust gas of plasma etching, Sep. Purif. Technol. 287 (2022), 120561.

[32] N. Xu, T. Yan, J. Li, L. Wang, D. Liu, Y. Zhang, A new TIFSIX anion pillared metal organic framework with abundant electronegative sites for efficient C_2H_2/CO_2 separation, Inorg. Chem. Front. 10 (2023) 522–528.

[33] L. Li, J. He, W. Xu, K. Zhang, T. Xing, Z. Li, D. Zhen, B. Xiong, Z. Ge, X. Zhang, S. Wang, F. Zhang, X. Gu, P. Dai, D. Liu, L. Yang, X. Zhao, High CO_2 separation performance on a metal-organic framework composed of nano-cages lined with an ultra-high density of dual-side open metal sites, Mater. Adv. 3 (2022) 493–497.

[34] Y. Hu, Y. Jiang, J. Li, L. Wang, M. Steiner, R.F. Neumann, B. Luan, Y. Zhang, New-generation anion-pillared metal-organic frameworks with customized cages for highly efficient CO_2 capture, Adv. Funct. Mater. 33 (2023) 2213915.

[35] X. Fu, Y. Wang, X. Zhang, Z. Zhang, C. He, Q. Liu, Fluorous metal-organic frameworks with unique cage-in-cage structures featuring fluorophilic pore surfaces for efficient C_2H_2/CO_2 separation, CCS Chem 4 (2022) 3416–3425.

[36] W. Fan, S. Yuan, W. Wang, L. Feng, X. Liu, X. Zhang, X. Wang, Z. Kang, F. Dai, D. Yuan, D. Sun, H.-C. Zhou, Optimizing multivariate metal-organic frameworks for efficient C_2H_2/CO_2 separation, J. Am. Chem. Soc. 142 (2020) 8728–8737.

[37] S. Chen, N. Behera, C. Yang, Q. Dong, B. Zheng, Y. Li, Q. Tang, Z. Wang, Y. Wang, J. Duan, A chemically stable nanoporous coordination polymer with fixed and free Cu^{2+} ions for boosted C_2H_2/CO_2 separation, Nano Res. 14 (2020) 546–553.

[38] J. Wang, Y. Zhang, Y. Su, X. Liu, P. Zhang, R.B. Lin, S. Chen, Q. Deng, Z. Zeng, S. Deng, B. Chen, Fine pore engineering in a series of isoreticular metal-organic frameworks for efficient C_2H_2/CO_2 separation, Nat. Commun. 13 (2022) 200.

[39] C. He, Z. Ye, Y. Xu, D. Zhou, H. Zhou, D. Chen, J. Zhang, X. Chen, Hyperfine adjustment of flexible pore-surface pockets enables smart recognition of gas size and quadrupole moment, Chem. Sci. 8 (2017) 7560–7565.

[40] W. Lou, J. Li, W. Sun, Y. Hu, L. Wang, R.F. Neumann, M. Steiner, Z. Gu, B. Luan, Y. Zhang, Screening Hoffman-type metal organic frameworks for efficient C_2H_2/CO_2 separation, Chem. Eng. J. 452 (2023), 139296.

[41] H. Li, C. Liu, C. Chen, Z. Di, D. Yuan, J. Pang, W. Wei, M. Wu, M. Hong, An unprecedented pillar-cage fluorinated hybrid porous framework with highly efficient acetylene storage and separation, Angew. Chem. Int. Ed. 60 (2021) 7547–7552.

[42] L. Liu, Z. Yao, Y. Ye, Y. Yang, Q. Lin, Z. Zhang, M. O'Keeffe, S. Xiang, Integrating pillared-layer strategy and pore-space partition method to construct multicomponent MOFs for C_2H_2/CO_2 separation, J. Am. Chem. Soc. 142 (2020) 9258–9266.

[43] Y. Zhang, L. Wang, J. Hu, S. Duttwyler, X. Cui, H. Xing, Solvent-dependent supramolecular self-assembly of boron cage pillared metal-organic frameworks for selective gas separation, CrystEngComm 22 (2020) 2649–2655.

[44] S.C. Fan, Y.T. Li, Y. Wang, J.W. Wang, Y.Y. Xue, H.P. Li, S.N. Li, Q.G. Zhai, Amide-Functionalized metal-organic frameworks coupled with open Fe/Sc sites for efficient acetylene purification, Inorg. Chem. 60 (2021) 18473–18482.

[45] X. Cui, K. Chen, H. Xing, Q. Yang, R. Krishna, Z. Bao, H. Wu, W. Zhou, X. Dong, Y. Han, B. Li, Q. Ren, M.J. Zaworotko, B. Chen, Pore chemistry and size control in hybrid porous materials for acetylene capture from ethylene, Science 353 (2016) 141–144.

[46] S. Yang, A.J. Ramirez-Cuesta, R. Newby, V. Garcia-Sakai, P. Manuel, S.K. Callear, S. I. Campbell, C.C. Tang, M. Schröder, Supramolecular binding and separation of hydrocarbons within a functionalized porous metal-organic framework, Nat. Chem. 7 (2015) 121–129.

[47] Y. Chen, Z. Qiao, H. Wu, D. Lv, R. Shi, Q. Xia, J. Zhou, Z. Li, An ethane-trapping MOF PCN-250 for highly selective adsorption of ethane over ethylene, Chem. Eng. Sci. 175 (2018) 110–117.

[48] Q. Hong, W. Wang, S. Chen, K. Chen, M. Liu, H.X. Zhang, J. Zhang, Host-guest pore space partition in a boron imidazolate framework for ethylene separation, Chem. Mater. 34 (2021) 307–313.

[49] P. Liao, W. Zhang, J. Zhang, X. Chen, Efficient purification of ethene by an ethane-trapping metal-organic framework, Nat. Commun. 6 (2015) 8697.

[50] X. Lei, H. Yang, Y. Wang, Y. Wang, X. Chen, Y. Xiao, X. Bu, P. Feng, Tunable metal-organic frameworks based on 8-connected metal trimers for high ethane uptake, Small 17 (2021), e2003167.

[51] L. Yang, X. Cui, Q. Yang, S. Qian, H. Wu, Z. Bao, Z. Zhang, Q. Ren, W. Zhou, B. Chen, H. Xing, A single-molecule propyne trap: highly efficient removal of propyne from propylene with anion-pillared ultramicroporous materials, Adv. Mater. 30 (2018), 1705374.

[52] Y. Jiang, L. Wang, T. Yan, J. Hu, W. Sun, R. Krishna, D. Wang, Z. Gu, D. Liu, X. Cui, H. Xing, Y. Zhang, Insights into thermodynamic-kinetic synergistic separation of propyne/propylene in anion pillared cage MOFs with entropy-enthalpy balanced adsorption sites, Chem. Sci. 14 (2023) 298–309.

[53] P. Liu, K. Chen, Y. Chen, X. Wang, J. Yang, L. Li, J. Li, Linker micro-regulation of a Hofmann-based metal-organic framework for efficient propylene/propane separation, Inorg. Chem. Front. 9 (2022) 1082–1090.

[54] Y. Ren, H. Xu, S. Gang, Y. Gao, X. Jing, J. Du, An ultra-stable Zr(IV)-MOF for highly efficient capture of SO_2 from SO_2/CO_2 and SO_2/CH_4 mixtures, Chem. Eng. J. 431 (2022), 134057.

[55] X. Cui, Q. Yang, L. Yang, R. Krishna, Z. Zhang, Z. Bao, H. Wu, Q. Ren, W. Zhou, B. Chen, H. Xing, Ultrahigh and selective SO_2 uptake in inorganic anion-pillared hybrid porous materials, Adv. Mater. 29 (2017), 1606929.

[56] L. Guo, F. Zheng, Q. Xu, R. Chen, H. Sun, L. Chen, Z. Zhang, Q. Yang, Y. Yang, Q. Ren, Z. Bao, Double-accessible open metal sites in metal-organic frameworks with suitable pore size for efficient Xe/Kr separation, Ind. Eng. Chem. Res. 61 (2022) 7361–7369.

[57] Y. Wu, W. Zhang, S. Chen, Y. Fu, T. Yan, W. Huang, Z. Zhang, B. Yang, H. Ma, Tuning surface inductive electric field in microporous organic polymers for Xe/Kr separation, Chem. Eng. J. 426 (2021), 131271.

[58] W. Gong, Y. Xie, T.D. Pham, S. Shetty, F.A. Son, K.B. Idrees, Z. Chen, H. Xie, Y. Liu, R.Q. Snurr, B. Chen, B. Alameddine, Y. Cui, O.K. Farha, Creating optimal pockets in a clathrochelate-based metal-organic framework for gas adsorption and separation: experimental and computational studies, J. Am. Chem. Soc. 144 (2022) 3737–3745.

[59] L. Li, L. Guo, Z. Zhang, Q. Yang, Y. Yang, Z. Bao, Q. Ren, J. Li, A robust squarate-based metal-organic framework demonstrates record-high affinity and selectivity for xenon over krypton, J. Am. Chem. Soc. 141 (2019) 9358–9364.

[60] Z. Niu, Z. Fan, T. Pham, G. Verma, K.A. Forrest, B. Space, P.K. Thallapally, A.M. Al-Enizi, S. Ma, Self-adjusting metal-organic framework for efficient capture of trace xenon and krypton, Angew. Chem. Int. Ed. 61 (2022), e202117807.

[61] L. Gong, Y. Ye, Y. Liu, Y. Li, Z. Bao, S. Xiang, Z. Zhang, B. Chen, A microporous hydrogen-bonded organic framework for efficient Xe/Kr separation, ACS Appl. Mater. Interfaces 14 (2022) 19623–19628.

[62] X.-L. Wu, Z.-J. Li, F.-D. Tang, N. Qian, X.-X. Chu, W. Liu, A novel fluorinated metal-organic framework for xenon/krypton separation, Chin. J. Struct. Chem. 40 (2021) 85–90.

[63] Y. Chen, K.B. Idrees, F.A. Son, X. Wang, Z. Chen, Q. Xia, Z. Li, X. Zhang, O.K. Farha, Tuning the structural flexibility for multi-responsive gas sorption in isonicotinate-based metal-organic frameworks, ACS Appl. Mater. Interfaces 13 (2021) 16820–16827.

[64] Z. Zhu, B. Li, X. Liu, P. Zhang, S. Chen, Q. Deng, Z. Zeng, J. Wang, S. Deng, Efficient Xe/Kr separation on two Metal-Organic frameworks with distinct pore shapes, Sep. Purif. Technol. 274 (2021), 119132.

[65] J.-Z. Wang, X.-P. Fu, Q.-Y. Liu, L. Chen, L.-P. Xu, Y.-L. Wang, Dinuclear nickel-oxygen cluster-based metal-organic frameworks with octahedral cages for efficient Xe/Kr separation, Inorg. Chem. 61 (2022) 5737–5743.

[66] X. Li, H. Bian, W. Huang, B. Yan, X. Wang, B. Zhu, A review on anion-pillared metal-organic frameworks (APMOFs) and their composites with the balance of adsorption capacity and separation selectivity for efficient gas separation, Coord. Chem. Rev. 470 (2022), 214714.

[67] B. Li, X. Cui, D. O'nolan, H.-M. Wen, M. Jiang, R. Krishna, H. Wu, R.-B. Lin, Y.-S. Chen, D. Yuan, H. Xing, W. Zhou, Q. Ren, G. Qian, M.J. Zaworotko, B. Chen, An ideal molecular sieve for acetylene removal from ethylene with record selectivity and productivity, Adv. Mater. 29 (2017), 1704210.

[68] S.K. Elsaidi, M.H. Mohamed, C.M. Simon, E. Braun, T. Pham, K.A. Forrest, W. Xu, D. Banerjee, B. Space, M.J. Zaworotko, P.K. Thallapally, Effect of ring rotation upon gas adsorption in SIFSIX-3-M (M = Fe, Ni) pillared square grid networks, Chem. Sci. 8 (2017) 2373–2380.

[69] Y. Jiang, J. Hu, L. Wang, W. Sun, N. Xu, R. Krishna, S. Duttwyler, X. Cui, H. Xing, Y. Zhang, Comprehensive pore tuning in an ultrastable fluorinated anion cross-linked cage-like MOF for simultaneous benchmark propyne recovery and propylene purification, Angew. Chem., Int. Ed. 61 (2022), e202200947.

[70] A.S. Dorcheh, D. Denysenko, D. Volkmer, W. Donner, M. Hirscher, Noble gases and microporous frameworks; from interaction to application, Microporous Mesoporous Mater. 162 (2012) 64–68.

[71] K.B. Idrees, Z. Chen, X. Zhang, M.R. Mian, R.J. Drout, T. Islamoglu, O.K. Farha, Tailoring pore aperture and structural defects in zirconium-based metal-organic frameworks for krypton/xenon separation, Chem. Mater. 32 (2020) 3776–3782.

[72] Y. Tao, Y. Fan, Z. Xu, X. Feng, R. Krishna, F. Luo, Boosting selective adsorption of Xe over Kr by double-accessible open-metal site in metal-organic framework: experimental and theoretical Research, Inorg. Chem. 59 (2020) 11793–11800.

[73] B. Liu, Y. Gong, X. Wu, Q. Liu, W. Li, S. Xiong, S. Hu, X. Wang, Enhanced xenon adsorption and separation with an anionic indium-organic framework by ion exchange with Co^{2+}, RSC Adv. 7 (2017) 55012–55019.

[74] Y.-S. Bae, B.G. Hauser, Y.J. Colón, J.T. Hupp, O.K. Farha, R.Q. Snurr, High xenon/krypton selectivity in a metal-organic framework with small pores and strong adsorption sites, Microporous Mesoporous Mater. 169 (2013) 176–179.

[75] Z. Yan, Y. Gong, B. Chen, X. Wu, Q. Liu, L. Cui, S. Xiong, S. Peng, Methyl functionalized Zr-Fum MOF with enhanced Xenon adsorption and separation, Sep. Purif. Technol. 239 (2020), 116514.

[76] H. Wang, Z. Shi, J. Yang, T. Sun, B. Rungtaweevoranit, H. Lyu, Y.-B. Zhang, O. M. Yaghi, Docking of Cu^{I} and Ag^{I} in metal-organic frameworks for adsorption and separation of xenon, Angew. Chem. Int. Ed. 60 (2021) 3417–3421.

[77] J. Zhou, T. Ke, F. Steinke, N. Stock, Z. Zhang, Z. Bao, X. He, Q. Ren, Q. Yang, Tunable confined aliphatic pore environment in robust metal-organic frameworks for efficient separation of gases with a similar structure, J. Am. Chem. Soc. 144 (2022) 14322–14329.

[78] P. Zhang, Y. Zhong, Q. Yao, X. Liu, Y. Zhang, J. Wang, Q. Deng, Z. Zeng, S. Deng, Robust ultramicroporous metal-organic framework with rich hydroxyl-decorated

channel Walls for highly selective noble gas separation, J. Chem. Eng. Data 65 (2020) 4018–4023.
[79] F.-A. Guo, K. Zhou, J. Liu, X. Lia, H. Wang, A microporous Zr_6@Zr-MOF for the separation of Xe and Kr Check for updates, Dalton Trans. 51 (2022) 10856–10859.
[80] T. Wang, Y.-L. Peng, E. Lin, Z. Niu, P. Li, S. Ma, P. Zhao, Y. Chen, P. Cheng, Z. Zhang, Robust bimetallic ultramicroporous metal-organic framework for separation and purification of noble gases, Inorg. Chem. 59 (2020) 4868–4873.
[81] R. Krishna, Metrics for evaluation and screening of metal-organic frameworks for applications in mixture separations, ACS Omega 5 (2020) 16987–17004.
[82] R. Krishna, Methodologies for evaluation of metal-organic frameworks in separation applications, RSC Adv. 5 (2015) 52269–52295.

Efficient Xe/Kr separation in fluorinated pillar-caged metal-organic frameworks

Jiahao Li,[a] Lingyao Wang*[a], Yuxin Chen,[a] Zonglin Gu*[b], Tao Jiang,[c] Binquan Luan*[d], Rajamani Krishna,[e] and Yuanbin Zhang*[a]

[a] Key Laboratory of the Ministry of Education for Advanced Catalysis Materials, College of Chemistry and Material Sciences, Zhejiang Normal University, Jinhua 321004, China.
[b] College of Physical Science and Technology, Yangzhou University, Jiangsu, 225009, China
[c] Department of Pharmacy, Jiangxi University of Chinese Medicine, Nanchang, 330004, China
[d] IBM Thomas J. Watson Research, Yorktown Heights, New York 10598, United States
[e] Van't Hoff Institute for Molecular Sciences, University of Amsterdam, Science Park 904, 1098 XH Amsterdam, Netherlands
* Corresponding authors.
Email address: lywang@zjnu.edu.cn (L. Wang), guzonglin@yzu.edu.cn (Z. Gu), bluan@us.ibm.com (B. Luan) and ybzhang@zjnu.edu.cn (Y. Zhang),

This PDF file includes:

Supplementary Text

Powder X-ray diffraction (PXRD) data were collected on the SHIMADZU XRD-6000 diffractometer (Cu Kαλ = 1.540598 Å) with an operating power of 40 KV, 30 mA and a scan speed of 4.0°/min. The range of 2θ was from 5° to 50°.

Thermal gravimetric analysis was performed on the TGA STA449F5 instrument. Experiments were carried out using a platinum pan under nitrogen atmosphere which conducted by a flow rate of 60 mL/min nitrogen gas. First, the sample was heated at 80 °C for 1 h to remove the water residue and equilibrated for 5 minutes, then cooled down to 50 °C. The data were collected at the temperature range of 50 °C to 600 °C with a ramp of 10 °C /min.

Grand canonical Monte Carlo (GCMC) simulations were performed in RASPA package [Dubbeldam, D.; Calero, S.; Ellis, D. E.; Snurr, R. Q., Raspa: Molecular Simulation Software for Adsorption and Diffusion in Flexible Nanoporous Materials. Mol. Simulat. 2016, 42 (2), 81-101.]. The structure of TIFSIX-Cu-TPA was firstly optimized via DFT geometry optimization (see detailed protocol below). Because both Xe and Kr atoms are charge neutral, no Coulomb interaction was calculated. For the van der Waals interaction, Lenna-Jones parameters for all aromatic C, H, N were taken from OPLS-AA force field, while parameters for the rest atoms were taken from the universal force field (UFF). Krypton (Kr) and xenon (Xe) were modeled as single spheres, with their parameters taken from previous studies [Hirschfelder, J. O.; Curtiss, C. F.; Bird, R. B. The Molecular Theory of Gases and Liquids; Revised.; Wiley-Interscience, 1964; Talu, O.; Myers, A. L. Colloid. Surface. A 2001, 187-188, 83-93]. The framework was considered to be rigid during the simulation and the interaction energy between the adsorbed molecules and the framework were computed through the Lennard-Jones 6-12 (LJ) potentials. The cutoff radius was chosen 12.8 Å for the van der Walls interaction.

Table S1. Crystallographic parameters of the TIFSIX-Cu-TPA, GeFSIX-Cu-TPA and NbOFFIVE-Cu-TPA.

Materials	TIFSIX-Cu-TPA	GeFSIX-Cu-TPA	NbOFFIVE-Cu-TPA
Cell	a=17.5855(9)	17.5352(3)	a=17.5990(5)
	b=17.5855(9)	17.5352(3)	b=17.5990(5)
	c=17.5855(9)	17.5352(3)	c=17.5990(5)
U	α=90	α=90	α=90
	β=90	α=90	β=90
	γ=90	γ=90	γ=90
Temperature	173 K	298 K	184 K
Volume ($Å^3$)	5438.3(8)	5391.8(3)	5450.8(5)
Space group	Pm-3n	Pm-3n	Pm-3n
Hall group	-P 4n 2 3	-P 4n 2 3	-P 4n 2 3
formula	$C_{20}H_{16}CuF_6N_{5.33}Ti$	$C_{20}H_{16}CuF_6GeN_{5.33}$	$C_{60}H_{48}Cu_3F_{15}N_{16}Nb_3O_3$
MW	556.49	581.21	1795.46
density	1.020	1.074	1.094
Z	6	6	2
R	0.0586(989)	0.1146(728)	0.0487(797)
wR2	0.1890(1137)	0.2588(878)	0.1458(924)
S	1.148	0.988	1.101
CCDC Nos.	2142633	2192744	2190367/2190959

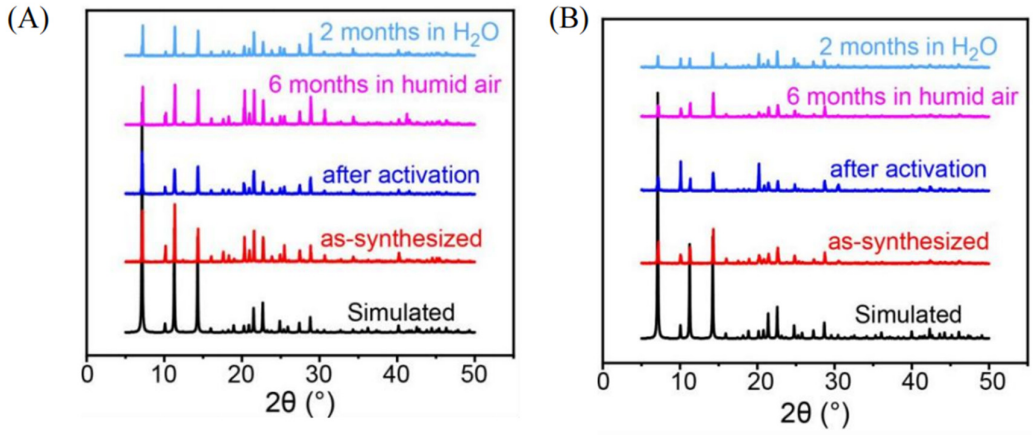

Figure S1. PXRD patterns of GeFSIX-Cu-TPA (A) and NbOFFIVE-Cu-TPA (B) after different treatments.

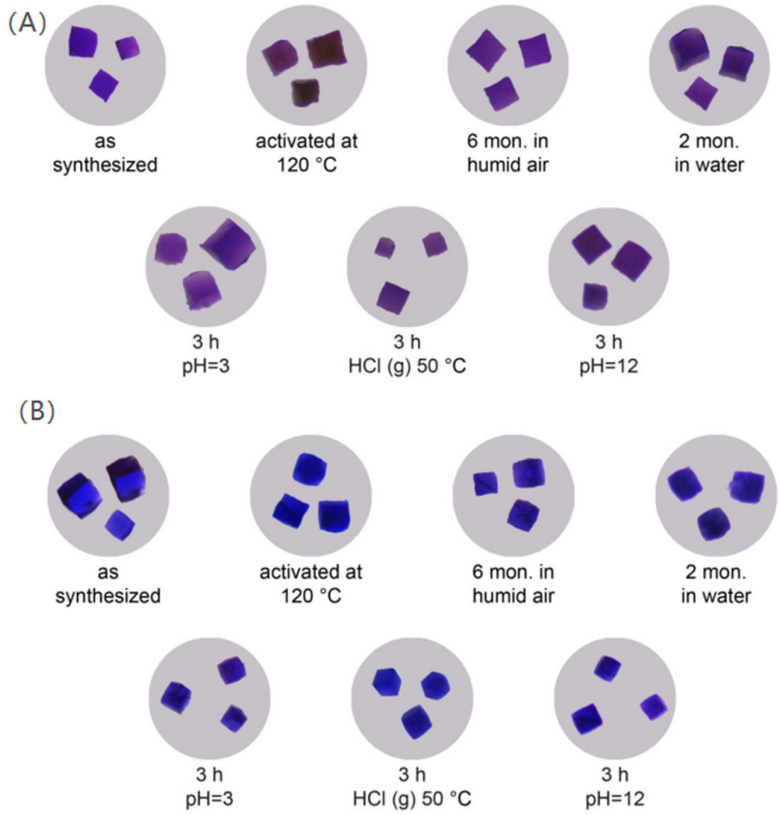

Figure S2. Photographs of singles of TIFSIX-Cu-TPA (A) and NbOFFIVE-Cu-TPA (B) after different treatments.

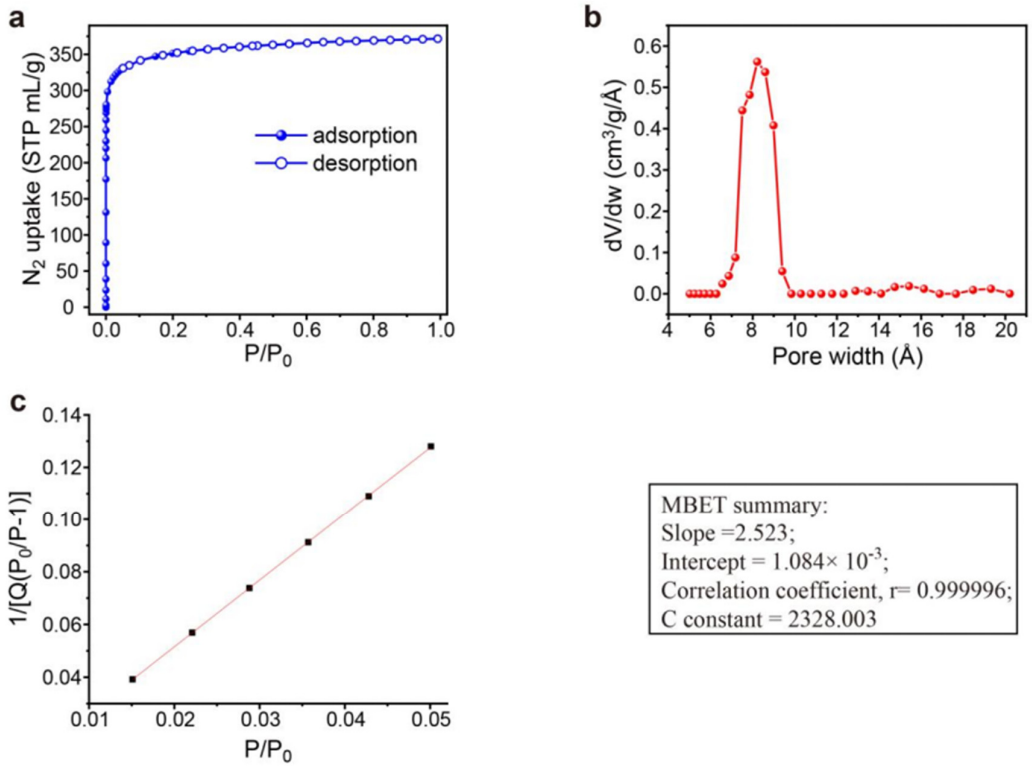

Figure S3. (a) The adsorption and desorption isotherm of N_2 on TIFSIX-Cu-TPA. (b) The calculated pore size distribution of TIFSIX-Cu-TPA. (c) Plot for the calculation of the BET surface area.

The BET surface area calculated from the N_2 adsorption isotherms under the pressure range of P/P_0 = 0.01-0.05 (for micropores) is 1380 m^2/g.

The total pore volume calculated from the N_2 adsorption isotherms is 0.575 cm^3/g.

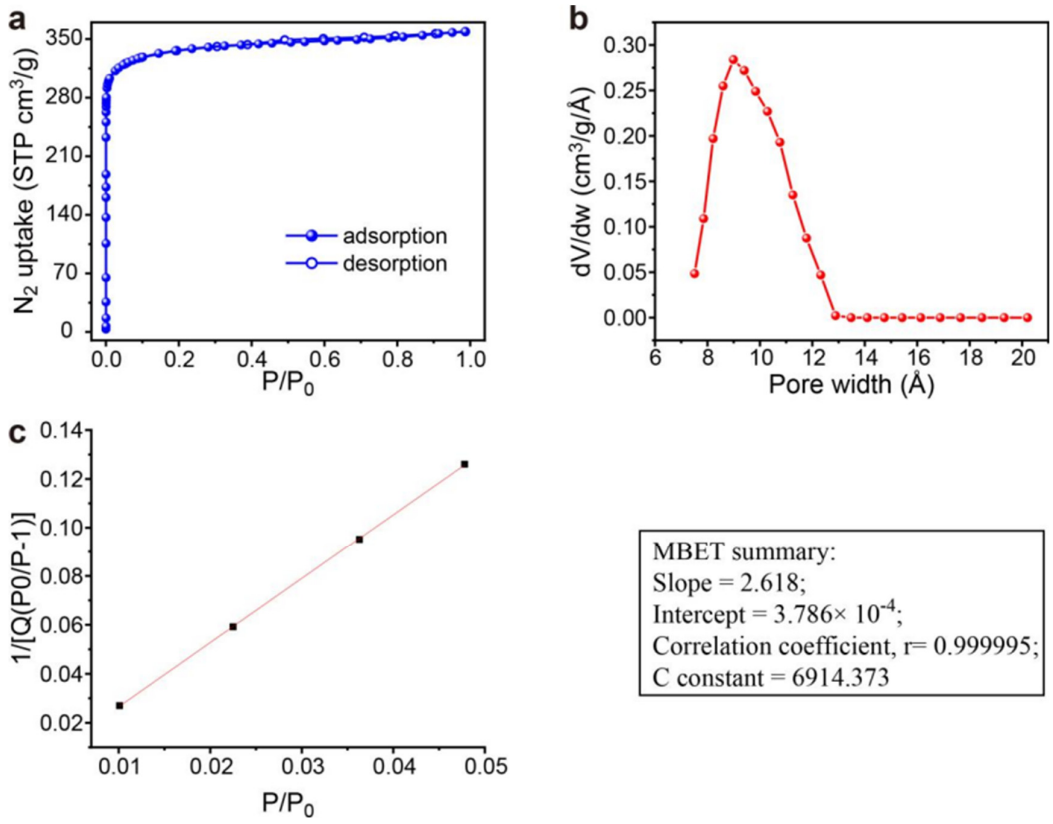

Figure S4. (a) The adsorption and desorption isotherm of N_2 on GeFSIX-Cu-TPA at 77 K. (b) The calculated pore size distribution of GeFSIX-Cu-TPA. (c) Plot for the calculation of the BET surface area.

The BET surface area calculated from the N_2 adsorption isotherms under the pressure range of P/P_0 = 0.01-0.05 (for micropores) is 1330 m^2/g.

The total pore volume calculated from the N_2 adsorption isotherms is 0.554 cm^3/g.

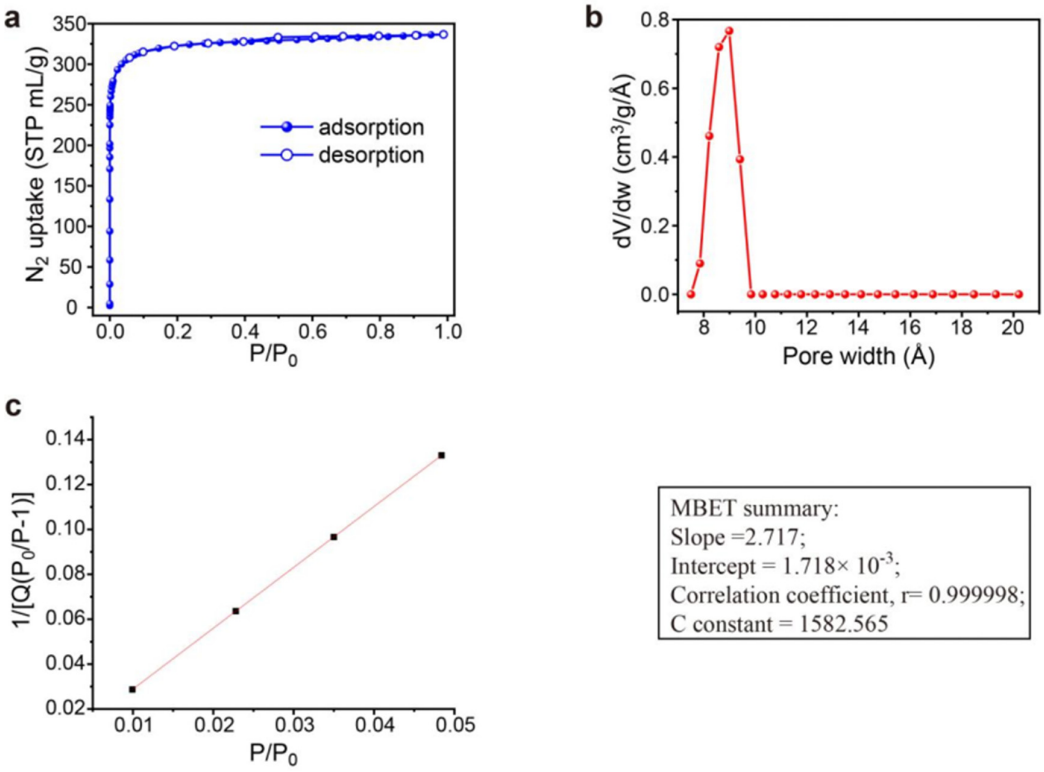

Figure S5. (a) The adsorption and desorption isotherm of N_2 on NbOFFIVE-Cu-TPA at 77 K. (b) The calculated pore size distribution of NbOFFIVE-Cu-TPA. (c) Plot for the calculation of the BET surface area.

The BET surface area calculated from the N_2 adsorption isotherms under the pressure range of P/P_0 = 0.01-0.05 (for micropores) is 1281 m^2/g.

The total pore volume calculated from the N_2 adsorption isotherms is 0.521 cm^3/g.

Table S2. Comparison of the BET surface and total pore volume of A-Cu-TPA.

	BET surface	The total pore volume

	(m^2/g)	(cm^3/g)
TIFSIX-Cu-TPA	1380	0.575
GeFSIX-Cu-TPA	1330	0.554
NbOFFIVE-Cu-TPA	1281	0.521

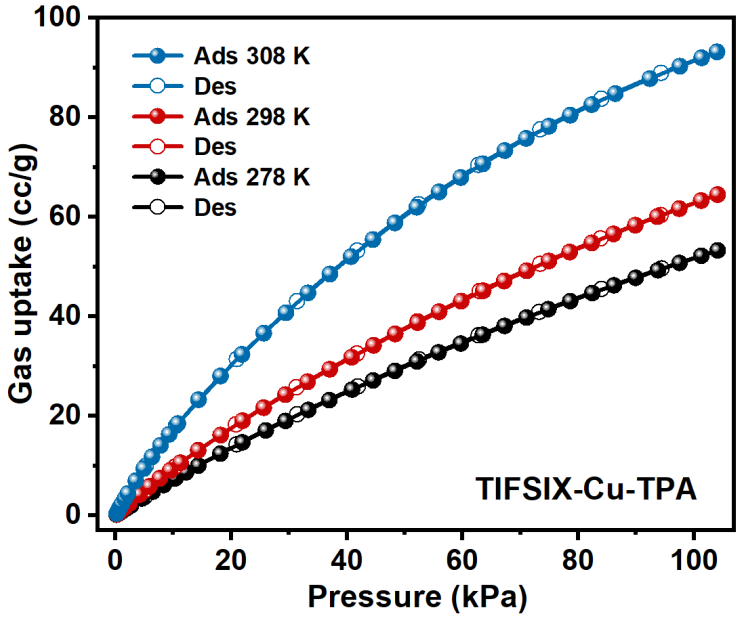

Figure S6. The adsorption and desorption isotherms of Xe on TIFSIX-Cu-TPA at 278 K, 298 K and 308 K.

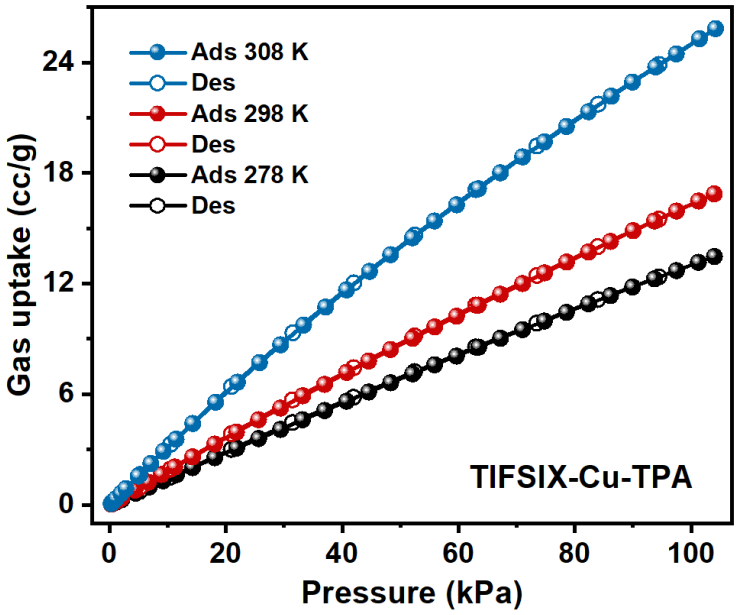

Figure S7. The adsorption and desorption isotherms of Kr on TIFSIX-Cu-TPA at 278 K, 298 K and 308 K.

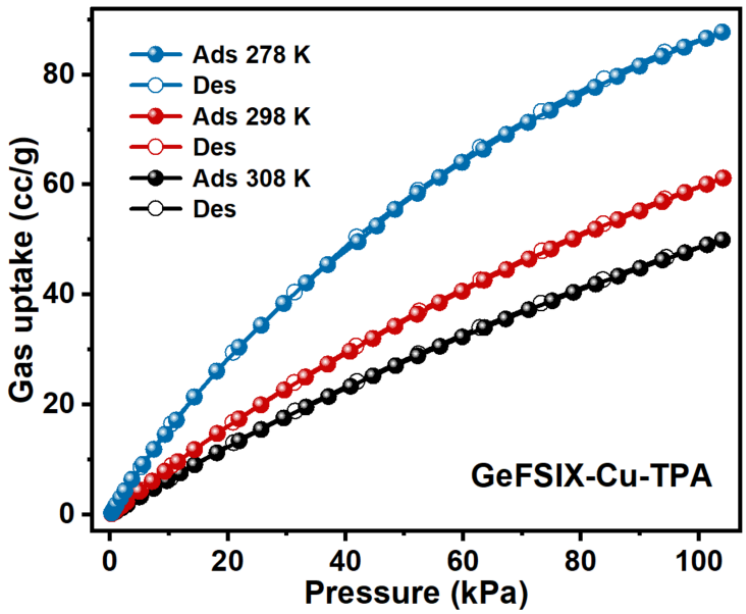

Figure S8. The adsorption and desorption isotherms of Xe on GeFSIX-Cu-TPA at 278 K, 298 K and 308 K.

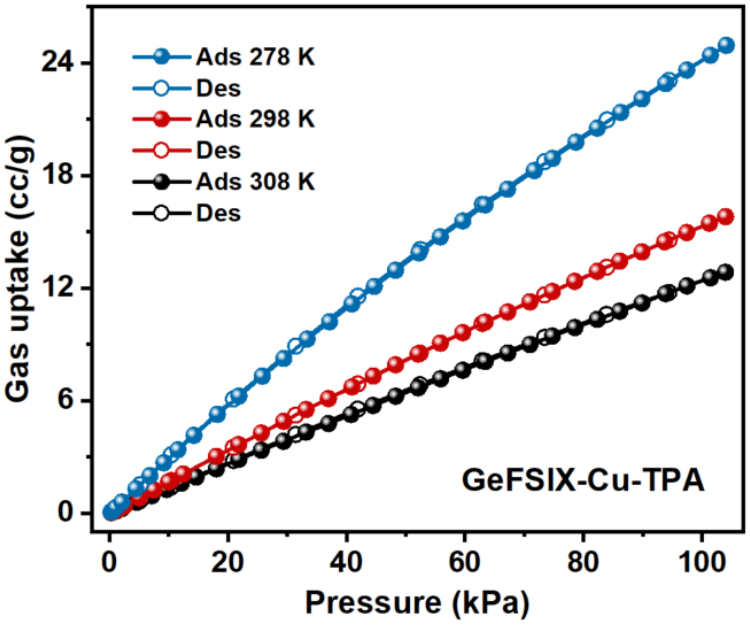

Figure S9. The adsorption and desorption isotherms of Kr on GeFSIX-Cu-TPA at 278 K, 298 K and 308 K.

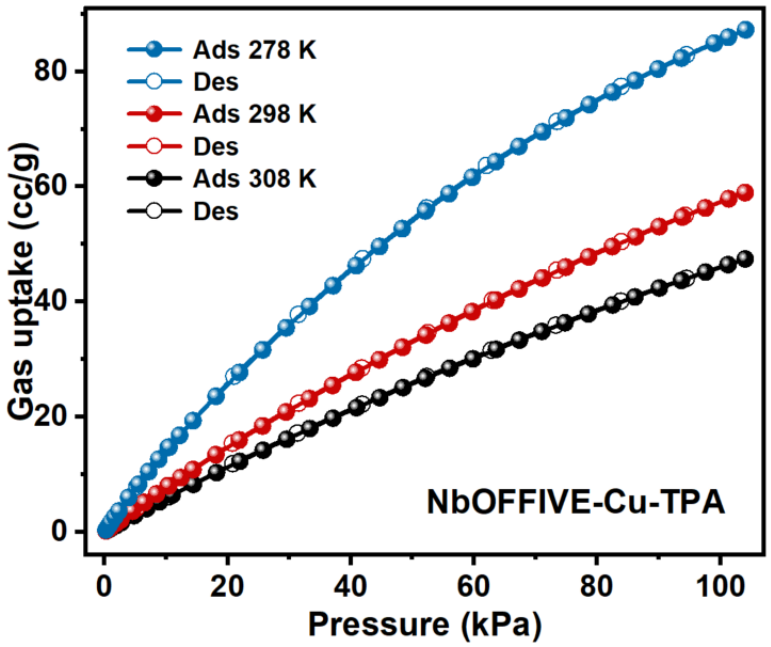

Figure S10. The adsorption and desorption isotherms of Xe on NbOFFIVE-Cu-TPA at 278 K, 298 K and 308 K.

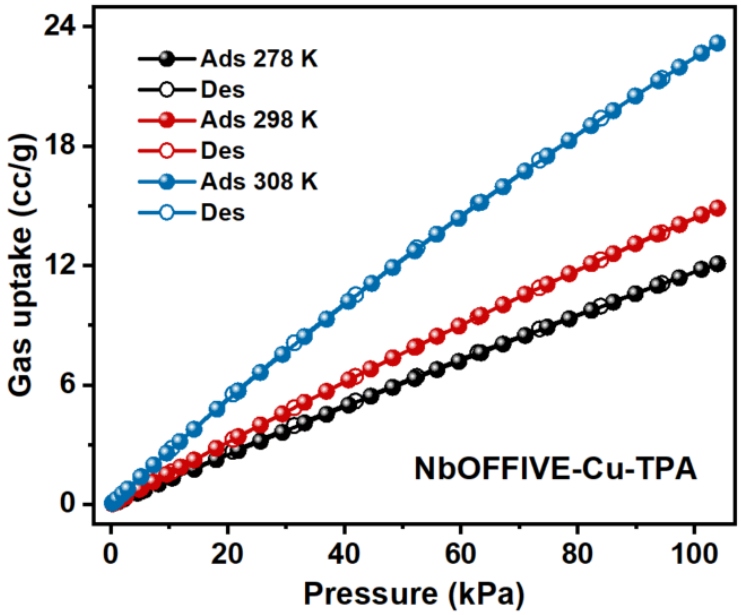

Figure S11. The adsorption and desorption isotherms of Kr on NbOFFIVE-Cu-TPA at 278 K, 298 K and 308 K.

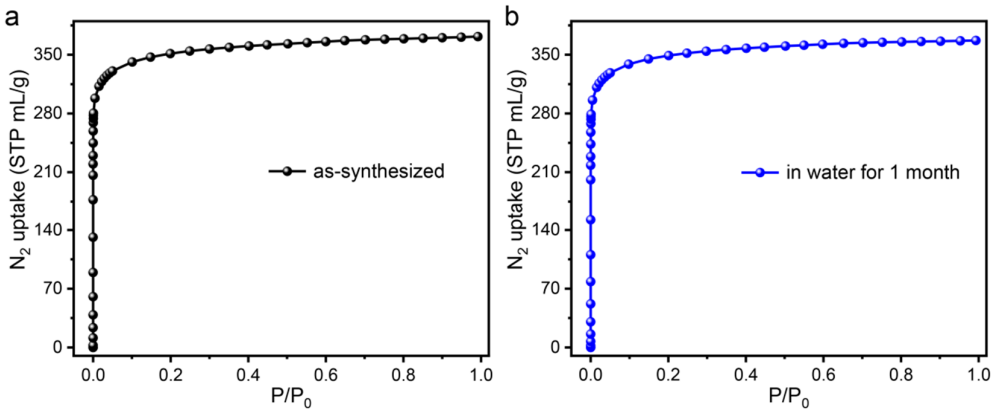

Figure S12. The adsorption isotherm of N_2 at 77 K on as-synthesized TIFSIX-Cu-TPA, and TIFSIX-Cu-TPA after soaking in water for 2 months.

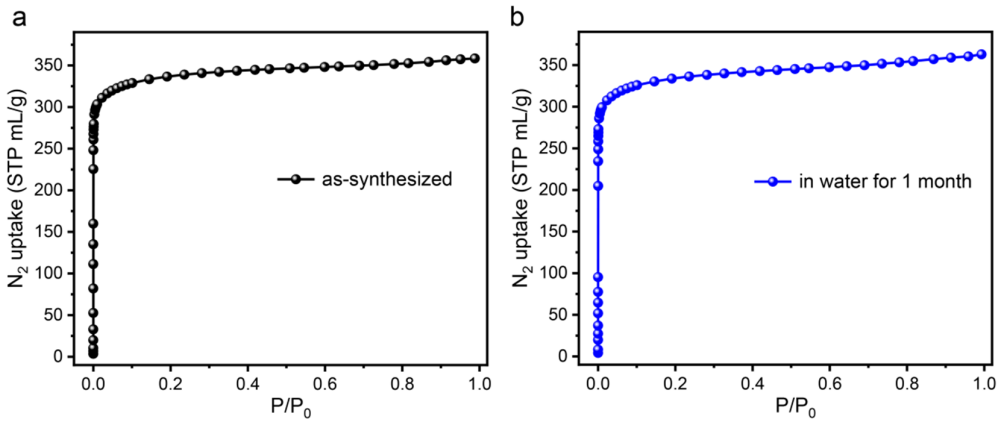

Figure S13. The adsorption isotherm of N_2 at 77 K on as-synthesized NbOFFIVE-Cu-TPA, and NbOFFIVE-Cu-TPA after soaking in water for 2 months.

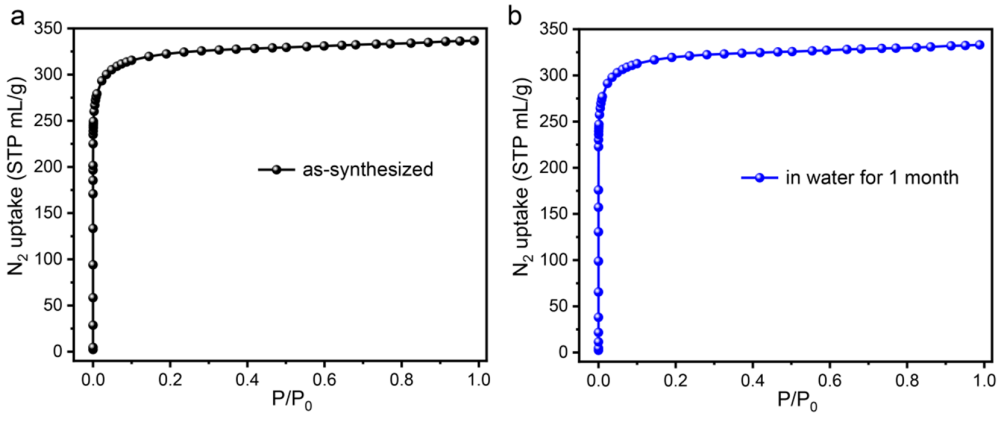

Figure S14. The adsorption isotherm of N_2 at 77 K on as-synthesized GeFSIX-Cu-TPA, and GeFSIX-Cu-TPA after soaking in water for 6 months.

Table S3. Xe Adsorption Capacity and Xe/Kr Selectivity for Various Materials at 298 K and 1 bar.

Adsorbents	Xe uptake ($cm^3\ g^{-1}$)	IAST $S_{(Xe/Kr)}$	Xe Q_{st}	Ref
TIFSIX-Cu-TPA	64.5	5.4	22	This work
GeFSIX-Cu-TPA	61.2	5.3	22.5	
NbOFFIVE-Cu-TPA	59	5.1	21.8	
Th-BPYDC-I	48.16	7.47	24	Dalton Trans. 51 (2022) 15233-15238
HIAM-401	43.8	7	32.7	Dalton Trans. 51 (2022) 10856-10859
$Ni(IN)_2$	72.76	17.7	29.22	J. Mater. Chem. A 10 (2022) 24824-24830
$Ni(AIN)_2$	66.61	20.32	30.95	
NOTT-102	49.28	3.9	/	J. Mater. Chem. A 3 (2015) 10747-10752
MOF-5	49.15	2.4	11.1	Ind. Eng. Chem. Res., 2009, 48, 3425-3431
$Co_3(C_4O_4)_2(OH)_2$	30	69.7	43.6	J. Am. Chem. Soc. 141 (2019) 9358-9364
UiO-66	44.44	5.9	24.6	Sep. Purif. Technol. 239 (2020) 116514
$Sr_4(TCPE)_2$	18.94	7	19.4	J. Solid State Chem., 288 (2020) 121337
Zr-Fum-Me	42.77	11.7	30.9	Sep. Purif. Technol., 239 (2020) 116514
SIFSIX-3-Cu	47.2	4.81 [b]	/	Nat. Commun. 11 (2020) 3103.
Y-csq-MOF-1	44.83	10.7 [a]	33.8	ACS Appl. Mater. Interfaces 9 (2017) 44560-44566
FJU-55	31.58	10	39.4	Nano Res. 15 (2022) 7559-7564
Co^{2+}-CPM-6	67.8	9.3	25.9	RSC Adv. 7 (2017) 55012-55019
CROFOUR-1Ni	40.17	22	37.4	Angew. Chem. Int. Ed. 55 (2016) 8285-8289
NU-403-PSDH	50.7	6.36	26	Chem. Mater.32 (2020) 3776-3782.
$Ni(4\text{-}DPDS)_2WO_4$	24.86	30.2	34.5	Angew. Chem. Int. Ed. 61 (2022) e202116686
ECUT-50a	50.62	8	32	Cryst. Growth Des.21 (2021) 954-959
UTSA-74	60.45	8.4	24.4	Inorg. Chem. 59 (2020) 11793-11800

ZIF-69	54.62	/	24.9	J. Radioanal. Nucl. Chem. 324 (2020) 1275-1281.
NKMOF-1-Ni	48.57	5.2	34.2	Inorg. Chem. 59 (2020) 4868-4873
$Co_3(HCOO)_6$	43.96	12 [a]	28	Chem. Sci. 5 (2014) 620-624
CaSDB	32.9	/	37	J. Mater. Chem. A 6 (2018) 11797-11803
Ca-SINAP-1	64.46	10.04	29.2	Inorg. Chem. 60 (2021) 1506-1512
SBMOF-2	63.87	10	26.4	J. Am. Chem. Soc. 137 (2015) 7007-7010
Cu-MOF-303	71.65	8.2	24.4	Angew. Chem. Int. Ed. 60 (2021) 3417-3421.
Ag-MOF-303	75	10.4	28.2	
MIL-120	44.59	9.6	31.5	J. Chem. Eng. Data 65 (2020) 4018-4023
ZUL-C2	57.57	19.1	28	J. Am.Chem. Soc. 144 (2022) 14322-14329
$Zn(ox)_{0.5}(trz)$	61.01	10.2	29	Inorg. Chem. 58 (2019) 15025-15028
Al-CDC	54.88	10.7	34.9	Sep. Purif. Technol. 274 (2021) 119132
SIFSIX-3-Zn	69.18	9.2	30	BMC Chem. Eng. 1 (2019) 3
NU-200	110	9.3	38	J. Am. Chem. Soc. 144 (2022) 3737-3745
Al-Fum-Me	67.42	10	/	Cryst. Growth Des. 20 (2020) 8039-8046
ZJU-74a-Pd	63	103.4	45.5	J. Am. Chem. Soc. 144 (2022) 3200-3209.
CopzNi	73.92	14	38.5	Ind. Eng. Chem. Res. 61 (2022) 7361-7369
MOF-Cu-H	71.65	16.7	33.3	J. Mater. Chem. A 6 (2018) 4752-4758.
Ni_2(m-dobdc)	124.79	10.1	28.3	Isr. J. Chem. 58 (2018) 1138-1143
Co_2(m-dobdc)	134.19	11.8	27.3	
ECUT-60	96.32	11.4	30	Sci. Bull. 66 (2021) 1073-1079
MOF-505	49.49	8	/	Microporous Mesoporous Mater. 169 (2013) 176-179
Ag@MOF-74-Ni	108.4	6.8	/	Chem. Commun. 50 (2014) 466-468

[a]: at a ratio of 1:9 (v/v); [b]: calculated from the breakthrough results.